Cover sheet for 'Response of atmospheric convection to surface drying: new insights from isentropic analysis'

Author 1: Laurel Régibeau-Rockett (Stanford University and National Research Council, laurelregibeau@gmail.com)

Author 2: Morgan O'Neill (University of Toronto, morgan.oneill@utoronto.ca)

Response of atmospheric convection to surface drying: new insights from isentropic analysis

Laurel Régibeau-Rockett[a,b] and Morgan E O'Neill[c]

[a] *Department of Earth System Science, Stanford University, Stanford, California, USA*

[b] *National Research Council, Monterey, California, USA*

[c] *Department of Physics, University of Toronto, Toronto, Canada*

Corresponding author: Laurel Régibeau-Rockett, laurelregibeau@gmail.com

ABSTRACT: There is strong evidence that the atmospheric moisture content of several solar system planets, including Earth, has varied over their lifetimes. A growing body of work also documents a range of atmospheric water vapor content on exoplanets. An improved understanding of the coupling between atmospheric moisture availability and convection could yield greater intuition about the past and current states of planetary atmospheres, including Earth's atmosphere. In this work, we investigate the changing heat engine behavior of localized radiative-convective equilibrium convection in a suite of moist-to-nearly-dry numerical simulations. Each simulation has a constant surface relative humidity, with values ranging from saturated to nearly dry surface conditions. We observe a deepening of the planetary boundary layer and a corresponding lifting of the cloud base under surface drying, in agreement with previous numerical and observational studies. The primary factor contributing to this is the reduction in the lifting condensation level temperature implied by the Clausius-Clapeyron relationship. Additionally, a diagnostic of the overall mass transport by atmospheric convection increases in drier conditions, consistent with prior work. This mainly results from an increase in planetary boundary layer convective mass transport. In contrast, free-tropospheric convective mass transport decreases, in agreement with previous studies. Finally, we find that surface evaporation is associated with less irreversible entropy production under surface drying and transitions from a spontaneous process to a non-spontaneous process. This occurs because near-surface air is more humid than the surface in the drier experiments, whereas in moister conditions the boundary layer is drier than the surface.

1. Introduction

It has long been accepted that moisture is an essential aspect of atmospheric convection on Earth. Compared to a dry atmosphere, for example, a moist atmosphere contains more intense updrafts due to latent heat release, and has narrower convective updrafts compared to the downwelling area. More recent work has demonstrated the far-reaching extent of atmospheric moisture's impacts on convection: Pauluis and Held (2002a) and Pauluis (2011) argued the atmosphere acts both as a heat engine that converts the atmosphere's differential heating into convective motions and as a dehumidifier. These two aspects of atmospheric convection are in competition with each other, with the atmosphere's action as a dehumidifier dominating over its behavior as a heat engine in an idealized moist atmosphere comparable to our own (Pauluis and Held 2002a). This contradicts the assumed dominance of the atmosphere's heat engine behavior in previous theories of moist convection (Rennó and Ingersoll 1996; Emanuel and Bister 1996).

The amount of moisture in our atmosphere has likely varied significantly over Earth's lifetime. For example, the Snowball Earth hypothesis posits that during the coldest portions of Earth's lifetime—particularly during subsets of the Neoproterozoic Era (1000–538.8 million years ago)—the Earth's surface was covered by an extensive layer of ice (e.g. Kirschvink 1992; Hoffman et al. 1998; Evans et al. 1997). Such an ice-covered surface combined with the cold atmosphere would imply a low atmospheric moisture content. Beyond Earth, mounting evidence suggests that moist convection may be important to the past and current evolution of solar system atmospheres, such as Venus (Kasting 1988), Mars (e.g. Wordsworth et al. 2013; Urata and Toon 2013), and Saturn (Li and Ingersoll 2015). Recent observations of exoplanets have also found significant levels of atmospheric water vapor (e.g. Tsiaras et al. 2019; Benneke et al. 2019; Roy et al. 2023; Mikal-Evans et al. 2023; Piaulet-Ghorayeb et al. 2024; Benneke et al. 2024). For example, many recent studies have focused on the atmospheric composition of the exoplanet K2-18b, with most studies in agreement that water vapor represents on the order of 0.01%-10% of its atmosphere by volume (e.g. Tsiaras et al. 2019; Benneke et al. 2019; Madhusudhan et al. 2020; Changeat et al. 2019). The number of observed exoplanets with expected water-containing atmospheres is likely to grow significantly, with several exoplanets considered as candidates for harboring significant water (e.g. Southworth et al. 2017; Cadieux et al. 2022; Piaulet et al. 2023; Cadieux et al. 2024). It seems likely that a large range of water-containing atmospheres exist in our universe, with varying amounts of atmospheric moisture. Understanding the impact of atmospheric moisture content on the characteristics of atmospheric convection could help us better understand the past evolution and present state of an array of different planetary atmospheres in the solar system and beyond—and most importantly, our Earth's atmosphere.

Previous work has demonstrated that more broadly, the atmospheric abundance of a condensable component is important to atmospheric convective characteristics (e.g. Mitchell et al. 2006; Hueso and Sánchez-Lavega 2006; Barth and Rafkin 2007; Pierrehumbert and Ding 2016; Mitchell and Lora 2016; Ding and Pierrehumbert 2016). While this condensable substance is water on Earth, this may not be the case on other planets. For example, Mitchell (2008) demonstrated, using axisymmetric simulations of Titan's atmosphere, that the atmosphere's characteristics are strongly sensitive to the initial supply of methane, which is the condensable component on Titan. The author found that below a threshold amount of initial methane, Titan's atmosphere abruptly shifted into a warmer state with much less precipitation and a shallower, more asymmetric Hadley cell. An investigation of the effect of atmospheric moisture on convective characteristics may have implications for convection in planetary atmospheres containing a condensable component that is not water.

A common idealized framework used to study the behavior of localized atmospheric convection is radiative-convective equilibrium (RCE). In the idealized modeling context, the term RCE refers to the statistically steady state of an idealized simulated atmosphere that experiences both net radiative cooling and surface heating. To date, a few studies have examined changes in atmospheric behavior between moist and dry RCE. Pauluis and Held (2002a,b) compared the characteristics of convection between moist and dry RCE in a cloud permitting model (CPM) using an entropy budget. In addition, both Mrowiec et al. (2011) and Wang and Lin (2020, 2021) studied differences in tropical cyclone properties between moist and dry RCE frameworks. A comparison of the characteristics of moist and dry RCE convection was also performed by Singh and O'Neill (2022).

The moist-to-dry transition itself has been extensively studied over both an ocean lower boundary (e.g. Mitchell et al. 2006, 2009; Zsom et al. 2012; Fan et al. 2021; McKinney et al. 2022; McKinney and Mitchell 2024; van der Drift and O'Gorman 2025) and land surfaces (Rochetin et al. 2014; McColl and Tang 2024). For example, Pauluis (2000) performed an entropy budget of moist-to-dry oceanic RCE convection in a CPM. The author found that from an energetic perspective, atmospheric convection retains moist behavior for most of the moist-to-dry transition, until the atmospheric moisture content has decreased by roughly 90%. This moist regime is characterized by the dominance of the energetic consumption of moist processes over the kinetic energy of convective motions and a greater portion of the total mechanical work dissipation occurring in shear zones surrounding falling hydrometeors rather than via the turbulent cascade. Later, Alland et al. (2017) investigated the impact of midlevel dry-air entrainment on oceanic tropical cyclones by applying Pauluis and Mrowiec (2013)'s technique of isentropic analysis to a suite of CPM ensembles initialized with different levels of atmospheric moisture. The ensembles initially had the same sea surface temperature and an identical subcloud vapor mixing ratio, but had different values of the initial moist entropy deficit above this point. The authors found no significant differences in the impacts of mid-level entrainment on the entropy of the eyewall updraft under atmospheric drying. However, the convective mass transport of the overturning circulation decreased under drying, implying that dry mid-level air may impact the tropical cyclone circulation via entrainment into the inflow layer. Another study by Spaulding-Astudillo and Mitchell (2023) varied the atmospheric saturation vapor pressure by a constant scaling factor in a suite of 1-D oceanic RCE simulations. A decreased saturation vapor pressure resulted in lower, warmer high cloud tops and a deeper planetary boundary layer. Finally, Cronin and Chavas (2019) investigated the moist-to-dry transition of atmospheric convection for the specific case of oceanic tropical cyclones. The authors found that their simulated tropical cyclones exhibited a more gradual transition from moist to dry characteristics compared to the findings of Pauluis (2000), although it should be noted that no tropical cyclones formed for their simulations with mid-to-low values of atmospheric moisture.

Some key differences exist between the moist-to-dry studies of Pauluis (2000) and Cronin and Chavas (2019), which could explain the contrast in the sharpness of the transition from moist to dry atmospheric behavior found in these works. First, whereas Pauluis (2000) investigated the moist-to-dry behavior of disorganized atmospheric convection, Cronin and Chavas (2019) studied tropical cyclones, which are highly organized systems. Organized convective systems may experience the moist-to-dry transition quite differently from localized convection. Second, Pauluis (2000) examined the moist-to-dry transition from the perspective of the atmosphere's behavior as a heat engine, with a focus on its changing energetics, whereas Cronin and Chavas (2019) examined changes in more "classical" tropical cyclone characteristics including their intensity and radius of maximum winds. Viewing atmospheric systems in terms of their thermodynamic behavior as heat engines, rather than in terms of these classical characteristics, could yield a different view on the changes in behavior of such systems over the transition. Finally, the construction of the moist-to-dry transition was different in these two studies. Whereas Cronin and Chavas (2019) varied the surface saturation specific humidity in their simulations, Pauluis (2000) varied the saturation specific humidity of the whole atmosphere. Such differences in the construction of the transition may have large impacts on the changing behavior of convection. For example, as noted by Pauluis (2000), his construction of the moist-to-dry transition results in hydrometeor fall velocities remaining at the same order of magnitude regardless of the reduction in hydrometeor water mass. This may have a strong impact on the variability of atmospheric cloud content as the atmosphere dries, resulting in an artificially steep decrease in cloud amounts. This could significantly affect the variability of atmospheric convection over the transition.

Pauluis and Mrowiec (2013) developed the procedure of "isentropic analysis". Isentropic analysis supports the computation of an alternative streamfunction of the atmospheric circulation cast into height and equivalent potential temperature space. This space has greater relevance to the thermodynamic behavior of the atmospheric heat engine compared to the classical Eulerian space in which convective streamfunctions are typically constructed. As such, this method can provide a new perspective on the response of atmospheric convection to changes in environmental thermodynamics, including temperature and moisture changes. Several previous works have employed isentropic analysis to study the behavior of atmospheric convection and convective systems in different contexts (e.g. Singh and O'Gorman 2015; Pauluis 2016; Mrowiec et al. 2016; Muller and Romps 2018; O'Neill and Chavas 2020; Li et al. 2023; Régibeau-Rockett et al. 2024). For example, some studies have employed a version of isentropic averaging developed for tropical cyclones (Mrowiec et al. 2016) to study the impacts of drying above the lifting condensation level on the secondary circulation of tropical cyclones (Alland et al. 2017), the evolution of tropical cyclones from an energetic perspective (Fang et al. 2019; Li et al. 2023), and tropical cyclone energetics in the mature state (Pauluis and Zhang 2017). Isentropic averaging has also been applied to both localized atmospheric convection (e.g. Pauluis and Mrowiec 2013; Pauluis 2016) and to organized convective systems (e.g. Mrowiec et al. 2015; Dauhut et al. 2017) to yield new understanding on the behavior of these systems. For example, Pauluis (2016) found that doubling the atmospheric carbon dioxide concentration results in a larger convective entropy transport. This results in a larger total energy production by the convective heat engine, although the partitioning of this energy between moist processes and the kinetic energy of convective motions does not significantly change.

In this study, we apply isentropic analysis to a suite of RCE CPM simulations with varying levels of surface moisture, where the moisture transition is constructed by varying the surface saturation mixing ratio as in Cronin and Chavas (2019). The goal of this analysis is to investigate how the thermodynamic behavior of localized convection varies as the available surface moisture decreases from fully moist conditions, without rotation. The paper is structured as follows: in section 2 we describe our suite of simulations and the analysis methodology, including a summary of the isentropic analysis method. In section 3, we present the results of our analyses. Finally, we provide a discussion of our results in section 4 and present some conclusions in section 5.

2. Methods

a. Model description

In this work, we analyze changes in atmospheric behavior in a suite of moist-to-near-dry simulations conducted using the Cloud Model 1 (CM1, Bryan and Fritsch 2002), version 21.1. In general, the design of our simulations emulates Singh and O'Gorman (2016), who performed an entropy budget on a suite of simulations over different sea surface temperatures in CM1 version 16 with added alterations. Their modifications to CM1 and the design of their simulations had the goal of conserving energy and mass well enough that their entropy budget could be closed within an acceptable margin of error. Although we do not perform an entropy budget in our work, we adopt a similar simulation design to improve the model's conservation of energy and mass.

All simulations are in a non-rotating 84 km $\times$ 84 km doubly-periodic domain. This domain size is smaller than the 200-300 km domain size required to support self-aggregation (Muller and Held 2012; Jeevanjee and Romps 2013). The domain has a 1-km horizontal grid spacing and a vertically stretched grid spacing (Wilhelmson and Chen 1982) ranging from 50 m at a height of 0 km to 500 m from 5.5 km up to the model top at 27 km. A Rayleigh damping layer is imposed in the top 3 km. The simulations are run with CM1's mesoscale modeling setup and the Yonsei University (YSU) planetary boundary layer parameterization (Hong et al. 2006). Microphysics is parameterized using the Morrison six-species double-moment scheme (Morrison et al. 2005,

2009) with hail as the large ice category. The radiation scheme is the RRTMG interactive scheme. Following Bretherton et al. (2005), we remove the diurnal and seasonal cycles from the radiative scheme via fixing the solar constant at 650.83 W m^{-2} and the solar zenith angle at 50.5°. We employ a Smagorinsky parameterization scheme for horizontal turbulence (Bryan and Rotunno 2009), a sixth-order hyper-diffusion scheme, and a sixth-order nondiffusive advection scheme. As in Singh and O'Gorman (2016), the sea surface temperature is set to 301.5 K. The simulations include dissipative heating and employ a set of equations for the moist microphysics that improves the conservation of energy and mass by accounting for the heat capacity of hydrometeors (Bryan and Fritsch 2002) and including the vertical transport of energy associated with hydrometeor sedimentation.

The surface layer is parameterized following the Weather Research and Forecasting model (WRF, Skamarock et al. 2008) MM5 scheme (Grell et al. 1994), as modified by Jiménez et al. (2012). We varied the surface dryness in our simulations by adding a scaling factor β to the surface saturation mixing ratio in the latent heat flux formula of the surface layer model following previous studies of the moist-to-dry transition (Mitchell et al. 2006, 2009; Cronin and Chavas 2019; Fan et al. 2021; McKinney et al. 2022):

$$LHF = \rho_1 L_{v,s} C_q U(\beta r_s^* - r_{v,1}). \tag{1}$$

Here, ρ_1 (kg m^{-3}) and $r_{v,1}$ (kg kg^{-1}) are the dry-air density and water vapor mixing ratio, respectively, in the surface layer (Jiménez et al. 2012). In CM1, this corresponds to the lowest model level of 25 m. U is the horizontal wind speed (m s^{-1}) at 10 m enhanced by a convective velocity as in Beljaars (1995) and a subgrid velocity following Mahrt and Sun (1995), r_s^* (kg kg^{-1}) is the saturation water vapor mixing ratio at the surface, and C_q is the dimensionless bulk transfer coefficient. The term $L_{v,s}$ (J kg^{-1}) is the latent heat of vaporization at the surface, defined as:

$$L_{v,s} = L_{v,0} + (c_{p,v} - c_{p,l})(T_s - T_{ref}),$$

where T_s (K) is the surface temperature, $L_{v,0}$ (J kg^{-1}) is the latent heat of vaporization at a reference temperature T_{ref} of 273.15 K, and $c_{p,v}$ and $c_{p,l}$ are, respectively, the specific heat capacities (J kg^{-1} K^{-1}) of water vapor and liquid water.

The term β in Eq. (1) is a dimensionless constant and controls the amount of available moisture that can exit the surface. This quantity can be thought of as the surface relative humidity and is related to the surface evaporative resistance, $\mathscr{R} = 100 \times (1 - \beta)$ (McKinney et al. 2022). A value of 1 corresponds to a typical surface moisture supply given the sea surface temperature of 301.5 K (i.e., a saturated or "fully moist" surface), whereas a low value is equivalent to a surface with a high evaporative resistance. Surface conditions resulting in a high evaporative resistance could include a high salinity and limited water (Fan et al. 2021). We vary β from 1 to 0.1 over the suite of simulations, which allows us to investigate the impacts of surface drying on localized RCE convection. We examine a range of β values from 1 to no lower than 0.1 because simulations with lower values of β did not achieve an RCE state within an 100-day time frame.

The simulations are initialized with small-amplitude thermal noise perturbations and vertical profiles of potential temperature and moisture computed from a period of 10 statistically steady days from the end of RCE simulations with an identical design and matching β values, but that are initialized with the Dunion (2011) moist tropical sounding. A similar initialization method was used in the moist-to-dry simulations of Cronin and Chavas (2019) and allows the system to adjust to the imposed surface conditions. The initialization simulations have a model top of 28 km, 1 km higher than the domain height of the main suite of simulations. This is due to CM1's requirement that input soundings must extend higher than the chosen model top. The upper-level Rayleigh damping layer thickness in these simulations matches that of the main set of simulations, and so the damping layer begins 1 km higher in the initialization simulations.

A total of five simulations are conducted, with β set to 1, 0.75, 0.5, 0.25, and 0.1. Following initialization simulations lasting between 32 and 83 days, with the time to RCE increasing as β decreases, the simulations reached a statistical equilibrium after approximately 50 days (Fig. 1). This RCE state was identified following the procedure described in Text S1 of the online supplemental materials. The presence of a statistically steady state after the point where RCE is first identified is confirmed by visual inspection of Hovmöller diagrams, constructed with daily data, of the vertical profile of equivalent potential temperature (θ_e) in each simulation (Fig. 1). In this work, θ_e is defined as in Bryan (2008) and following its formulation in CM1:

$$\theta_e = T(\frac{p_{ref}}{p_d})^{\frac{R_d}{c_{p,d}}} \mathscr{H}^{-\frac{r_v R_v}{c_{p,d}}} \exp\left[\frac{r_v L_{v,0}}{c_{p,d} T}\right],$$

where T is the temperature (K), p_{ref} = 1000 hPa is the reference pressure, p_d is the partial pressure of dry air (hPa), R_d is the gas constant for dry air (J kg^{-1}K^{-1}), R_v is the water vapor gas constant (J kg^{-1}K^{-1}), $c_{p,d}$ (J kg^{-1}K^{-1}) is the specific heat capacity of dry air, r_v is the water vapor mixing ratio (kg kg^{-1}), and $\mathscr{H}$ is the relative humidity with respect to liquid water:

$$\mathscr{H} = \frac{e_p}{e_s},$$

where e_p is the water vapor pressure (Pa) and e_s (Pa) is the saturation vapor pressure of Bolton (1980).

Once statistical equilibrium was achieved, we ran the simulations for a further 20 days with output data every 4 hours. The beginning of each of these 20-day periods is denoted by the vertical black lines in Fig. 1. In what follows, we apply isentropic analysis to these 20-day periods, as will be described in section 2b.

b. A Summary of Isentropic Analysis

In this work, we apply isentropic analysis to 20-day steady-state periods from each of the simulations described above. In our work, isentropic analysis is broken into the following steps (Pauluis 2016):

1. Compute the isentropic-average[1] vertical mass flux $\langle \rho w \rangle (z, \theta_e)$ (kg m^{-2} s^{-1} K^{-1}) following Eq. (1) of Pauluis and Mrowiec (2013). $\langle \rho w \rangle$ is the time- and horizontal-average of the vertical mass flux at a given height z that was binned by the corresponding equivalent potential temperature value θ_e.

[1] Although the standard nomenclature for this and other procedures involved in isentropic analysis uses the term "isentropic", these computations do not involve constant-entropy conditions.

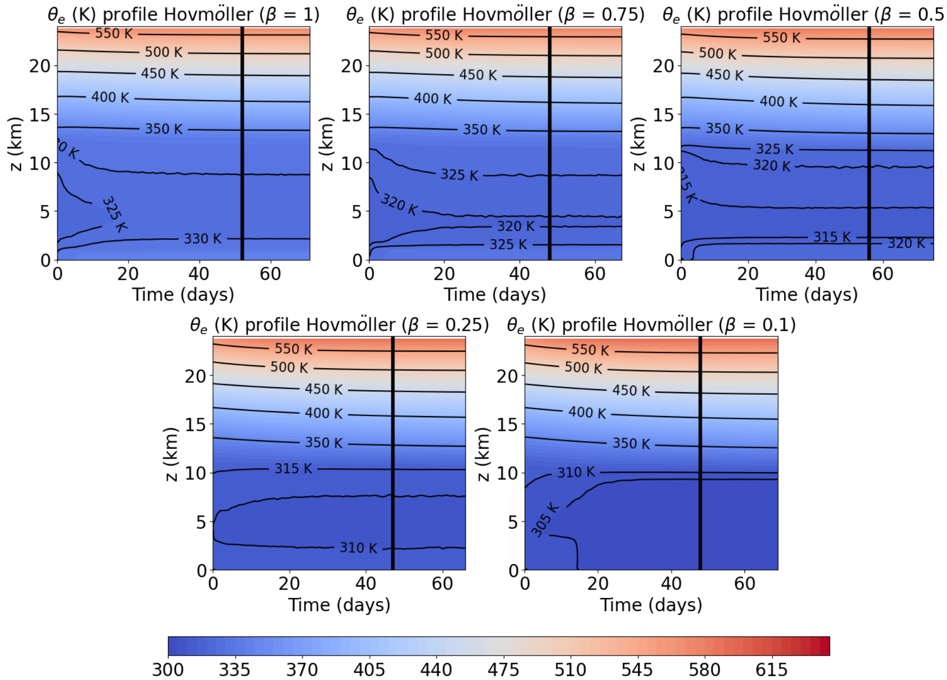

Fig. 1. Hovmöller plots of the time- and horizontal-mean vertical profiles of equivalent potential temperature (colors) in each constant-β simulation. Values from within the model sponge layer are not shown. The black vertical line denotes the start of the 20-day steady-state period that we analyze for each simulation.

2. Use $\langle \rho w \rangle$ to compute the isentropic streamfunction $\psi(z, \theta_e)$ (Fig. 2) following Eq. (3) of Pauluis and Mrowiec (2013). For given values of z and θ_e, $\psi(z, \theta_e)$ is the cumulative isentropic-average vertical mass flux for equivalent potential temperature values less than or equal to θ_e.

3. Use the isentropic streamfunction to construct a set of representative thermodynamic trajectories. When plotted as a contour plot with N equally-spaced levels, $\psi(z, \theta_e)$ is represented as a set of closed loops in $z - \theta_e$ space (Fig. 2). The isentropic analysis method implicitly assumes that these closed loops represent the mean trajectories of real air parcels in the atmospheric system. This assumption was shown to hold reasonably well in the context of axisymmetric tropical cyclones in Régibeau-Rockett et al. (2024).

4. Compute the mass-weighted isentropic-average values of thermodynamic quantities f, such as the absolute temperature and moist entropy: $\tilde{f} = \langle \rho f \rangle / \langle \rho \rangle$.

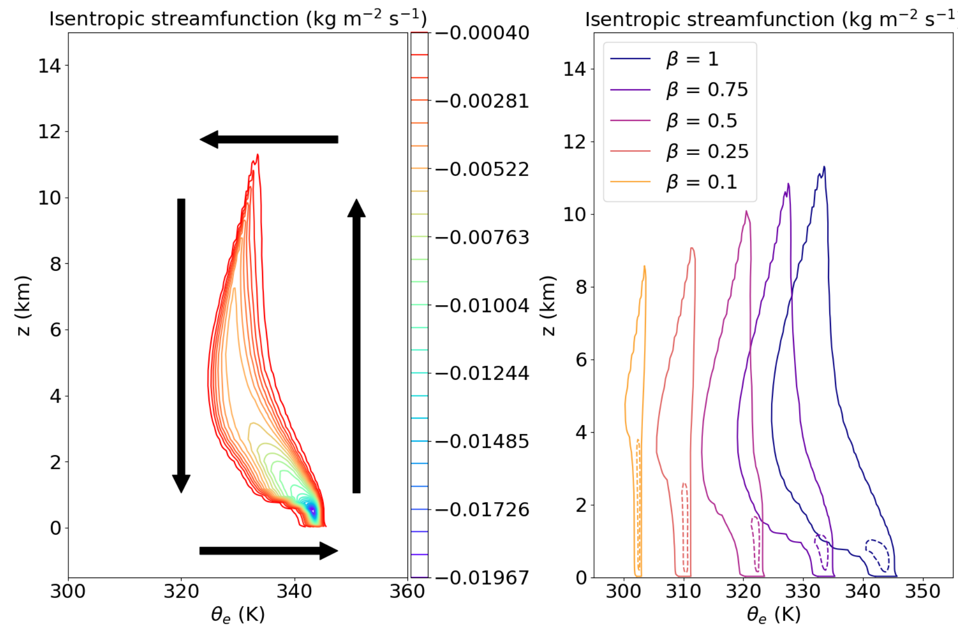

FIG. 2. Left: Isentropic streamfunction, $\psi(z,\theta_e)$, obtained from the 20-day steady state period of the β = 1 simulation. Black arrows show the direction of the thermally direct overturning circulation in $z-\theta_e$ space. Right: Comparison of the deepest trajectories (solid lines) derived from ψ during the 20-day steady-state period of each simulation. Also shown are the median trajectories (dashed lines).

5. Interpolate these mass-weighted isentropic-average thermodynamic quantities $\tilde{f}$ onto the constructed trajectories. The result is a projection of the isentropic streamfunction into different thermodynamic spaces, such as temperature-entropy space. Projecting the isentropic streamfunction into different spaces in this way can provide a new perspective on the influence of environmental changes on the atmospheric convection.

3. Results

In this section, we present the results of applying the isentropic analysis to 20-day steady-state periods from each of the constant-β simulations. We begin by presenting the transition of the atmospheric circulation in response to surface drying viewed in terms of the isentropic streamfunction. This streamfunction is then projected into different thermodynamic spaces, which yields additional insight on the changing behavior of the atmospheric circulation over the transition.

Because our work investigates the impact of the atmospheric moisture content on convective dynamics, our results may be sensitive to our choice of microphysical scheme. We checked the sensitivity of our results to the microphysics parameterization by running two suites of simulations identical to those discussed in section 2, but that had different representations of microphysics: the first suite employed the Thompson microphysics scheme (Thompson et al. 2008; Thompson and Eidhammer 2014), whereas the second used the double-moment graupel-and-hail NSSL microphysics parameterization (Ziegler 1985; Mansell et al. 2010; Mansell and Ziegler 2010). We also examined the sensitivity of our results to the planetary boundary layer (PBL) parameterization in two suites of sensitivity simulations. The first suite used the Mellor-Yamada-Nakanishi-Niino (MYNN) level 2.5 PBL scheme (Nakanishi and Niino 2006, 2009; Olson et al. 2019), while the second used the NCEP Global Forecast System scheme (GFS-EDMF, Hong and Pan 1996). More information on these sensitivity tests, together with the results of analyzing these simulation suites, can be found in Texts S2 and S3 and in Tables 1 and 2. In general, we find that the results presented in this section are not qualitatively sensitive to the microphysical or PBL schemes, although the magnitudes of some results do show sensitivity (entries marked with a * in Tables 1 and 2). Henceforth, we will note instances where a result is qualitatively sensitive to these parameterizations.

a. Effects of Moisture on the Isentropic Streamfunction

Figure 2 presents changes in selected trajectories from the isentropic streamfunction over the suite of simulations. We show here changes in both the deepest trajectory and a median trajectory, defined as the twelfth of 25 levels used to plot ψ in step 3 of the isentropic averaging process described in section 2b. The changes in the isentropic streamfunction reveal changes in the characteristics of the atmospheric circulation: first, as the surface dries, the depth of the circulation decreases (Table 1). In addition, the range of equivalent potential temperatures sampled by the circulation decreases, with more similar values of θ_e for updrafts and downwelling air (Table 1). This is unsurprising, since a smaller difference in θ_e between rising and sinking air is characteristic of dry convection. As β decreases, we also observe an increase in the depth of the PBL, or equivalently an increase in the lifting condensation level (LCL) (Table 1). In Fig. 2, the LCL is the level at which the θ_e range of the isentropic circulation noticeably increases, with the PBL below represented by the region in

Table 1. Changes in different metrics, derived from the isentropic streamfunction, from the $\beta = 1$ simulation to the $\beta = 0.1$ simulation. The metrics are: diagnosed cloudtop height (z_{top}) and temperature (T_{top}); mean difference in θ_e and vapor mixing ratio between updrafts and downdrafts for the deep trajectory ($\theta_{e,u-d}$ and $r_{v,u-d}$); percentage difference between vertical profiles of the relative humidity derived from the updraft and the downdraft of the deep trajectory below the diagnosed lifting condensation level (LCL) ($\mathscr{H}_{GG,u-d,PBL}$), where the percentage difference is computed with respect to the downdraft profile and the relative humidity is with respect to both liquid water and ice as in Goff and Gratch (1946); height and temperature of the diagnosed LCL (z_{LCL} and T_{LCL}); change in moist entropy and total mixing ratio from the diagnosed LCL to the diagnosed cloudtop for the deep trajectory (δs_{up} and $\delta r_{T,up}$); change in Gibbs free energy of water vapor from the surface to the diagnosed LCL during the updraft leg of the deep trajectory ($\delta g_{v,LCL-surf}$); mean Gibbs free energy of water vapor for the near-surface portion of the deep trajectory ($g_{v,ns}$); change in water vapor Gibbs free energy from surface evaporation ($\Delta g_{v,s}$); irreversible entropy production from surface evaporation (ΔS_{surf}); and isentropic mass circulation ($\Delta\psi$). Except $\mathscr{H}_{GG,u-d,PBL}$, percentages are computed with respect to the value of each metric in the $\beta = 1$ simulation. Some results that depend on θ_e are recomputed using Marquet (2011)'s entropy potential temperature. Because not all results will be impacted by this change, only those that could be affected are shown. Due to the shape of the trajectories yielded by this method (Fig. S37), δs_{up} may not accurately capture changes in the entropy for deep convective updrafts. The magnitude of changes in some metrics varies substantially across the sensitivity tests, although their sign remains consistent. These metrics are marked with a *.

Metric	Main	Thompson	NSSL	MYNN	GFS	Marquet
Δz_{top} (km)	-2.7	-2.9	-3.3	-3.5	-3.4	-
$\Delta\theta_{e,u-d}$ (%)	-80	-77	-79	-82	-84	-70
Δz_{LCL} (km)	2.9	2.9	2.9	2.9	2.8	3.3
$\Delta(\Delta\psi)$ (%) *	80	83	120	150	240	130
ΔT_{LCL} (K)	-31	-31	-31	-31	-32	-
$\Delta\delta s_{up}$ (%)	-93	-90	-92	-95	-94	-79
$\Delta r_{v,u-d}$ (%)	-80	-78	-80	-82	-84	-
$\Delta\delta r_{T,up}$ (%)	-85	-84	-84	-85	-85	-
$\Delta\mathscr{H}_{GG,u-d,PBL}$ (%) *	13	8.9	8.8	11	7.4	-
$\Delta\delta g_{v,LCL-surf}$ (%)	580	560	560	540	530	-
$\Delta g_{v,ns}$ (%)	510	480	480	530	480	-
$\Delta(\Delta S_{surf})$ (mW m^{-2} K^{-1})	-4.7	-4.2	-4.3	-4.4	-5.0	-
$\Delta(\Delta g_{v,s})$ (%)	-190	-210	-210	-190	-180	-
ΔT_{top} (K) *	0.37	1.3	3.3	6.8	6.0	-

TABLE 2. Changes in different metrics not derived using the isentropic streamfunction from the $\beta = 1$ simulation to the $\beta = 0.1$ simulation. The metrics are: mean upward vertical mass flux within and above the PBL ($\Delta\rho w^+_{PBL}$ and $\Delta\rho w^+_{non-PBL}$); net radiative cooling (Q_{rad}); surface sensible and latent heat fluxes (SHF and LHF); height and temperature of the tropopause (z_{trop} and T_{trop}); and mean precipitation rate. All percentages are computed with respect to the value of each metric in the $\beta = 1$ simulation. Also shown are changes in mixed-layer CAPE and CIN (MLCAPE and MLCIN) from the $\beta = 1$ simulation to the $\beta = 0.25$ simulation. In all sensitivity suites, the level of free convection does not exist in the $\beta = 0.1$ simulation, so MLCAPE and MLCIN are undefined. The magnitude of changes in some metrics varies substantially across the sensitivity tests, although their sign remains consistent. These metrics are marked with a *.

Metric	Main	Thompson	NSSL	MYNN	GFS
ΔQ_{rad} (%)	-54	-56	-49	-57	-55
$\Delta\lvert Q_{rad}\rvert$ (W m^{-2})	-49	-47	-42	-54	-51
Δ SHF (W m^{-2})	28	27	31	27	29
Δ LHF (W m^{-2})	-78	-74	-74	-75	-79
$\Delta\rho w^+_{PBL}$ (%) *	2000	1900	3800	2400	3100
$\Delta\rho w^+_{non-PBL}$ (%) *	-36	-10	-24	-62	-8.1
Δ MLCAPE (J kg^{-1})	-1600	-1400	-1300	-1600	-1600
Δ MLCIN (J kg^{-1})	12	15	9.7	14	14
Δ precipitation rate (%)	-95	-99	-98	-95	-96
ΔT_{trop} (K)	-1.6	0.69	0.37	-0.36	0.058
Δz_{trop} (km)	-2.5	-3.0	-3.0	-2.5	-2.5

which rising air has a similar equivalent potential temperature value as sinking air. This is because the LCL is the level at which latent heat begins to be released by rising air parcels. Here, the LCL's height is diagnosed based on the characteristics of the isentropic streamfunction and is not necessarily equivalent to the thermodynamic LCL.

We next study the variability of the isentropic mass transport, $\Delta\psi$ (kg m^{-2} s^{-1}). The quantity $\Delta\psi$ is the mass transport in each of the N equally-spaced levels of the isentropic streamfunction, defined following Pauluis (2016) as $\Delta\psi = -N^{-1}\psi_{min}$, where ψ_{min} is the minimum value of ψ. By construction, this is the same for each level of the isentropic streamfunction. As can be seen in Fig. 3, $\Delta\psi$ increases by 80% between the fully moist and driest simulations (Table 1). Note that the percentage change in mass circulation is computed with respect to its value in the fully moist simulation. Because $\Delta\psi$ represents the mass transport of each level of the isentropic streamfunction, with high-θ_e air rising and low-θ_e air sinking, the increase in $\Delta\psi$ should indicate an increase in the

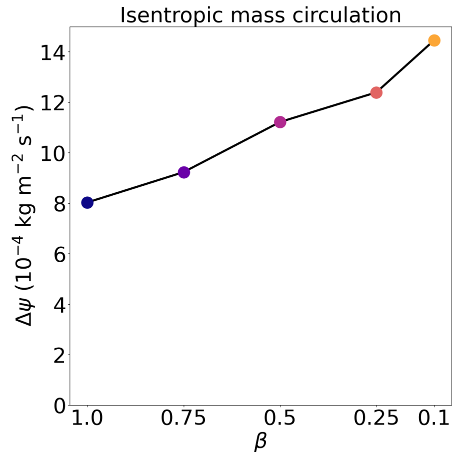

FIG. 3. Isentropic mass circulation $\Delta\psi$, computed during the 20-day steady-state periods from each simulation, versus β.

convective heat transport. However, in our simulations, the radiative cooling rate and total surface heat flux in the domain, computed as described in the appendix, decrease strongly as the surface dries (Fig. 4, Table 2). In RCE, these quantities are balanced by the convective heat transport, implying that the heat transport also decreases as the atmosphere dries. This is not incompatible with the increase in the convective mass transport because the heat transport is also dependent on the difference in θ_e between the updraft and downwelling air. This difference decreases significantly with decreasing β (Fig. 2, Table 1), and so acts to decrease the convective heat transport. Overall, the decrease in the updraft/downwelling θ_e difference outweighs the increased convective mass transport in terms of its impact on the convective heat transport, resulting in the lower convective heat transport that we observe under surface drying. It is interesting to note, however, that the decline in the external heating and cooling of the atmosphere under drying is sufficiently slow compared to the narrowing of the updraft-downdraft difference in θ_e that the circulation must intensify to maintain a sufficiently large convective heat transport.

Although the convective mass transport increases overall, shallow and deep convection may respond quite differently to imposed surface drying. We next examine changes in the mean upward mass flux, ρw^+, for the PBL and for the region above the PBL separately (Fig. 5, Table 2). The former is a proxy for changes in shallow convection, while the latter represents changes in the deep convective mass flux. Here, the PBL height is not diagnosed based on the characteristics of the isentropic streamfunction as in the rest of the text. Instead, we use the PBL height that is output

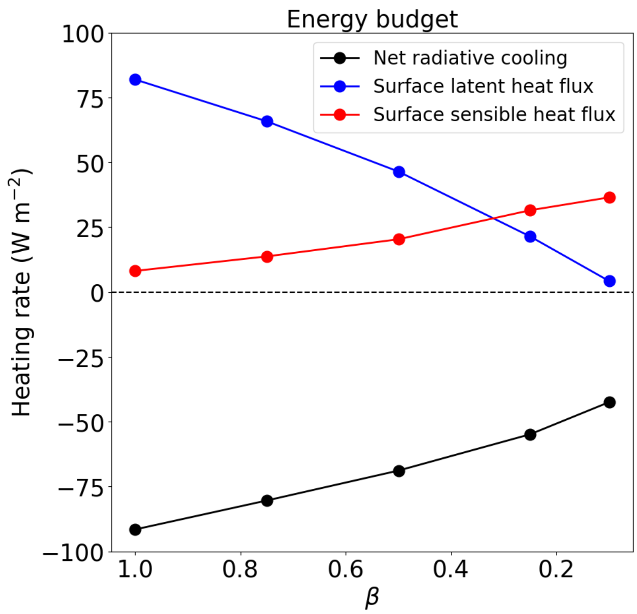

FIG. 4. Time-mean, domain-integrated radiative heating rate divided by the area of the surface (black line), and time- and horizontal-mean surface latent (blue line) and sensible (red line) heat fluxes, computed during the 20-day steady-state periods from each simulation, versus β.

from CM1. The mass transport by shallow convection strongly increases under surface drying, while the mass transport by deep convection decreases. Hence, the increase in the isentropic mass circulation is the result of a strong increase in shallow convective mass transport.

The decrease in the deep convective mass flux due to drying may be explained by considering changes in the Mixed-Layer Convective Available Potential Energy (MLCAPE) and Convective Inhibition (MLCIN). The MLCAPE decreases strongly as the surface dries (Table 2), implying that the environment becomes less favorable to deep convection, consistent with our results. Meanwhile, the MLCIN grows significantly (Table 2), implying a reduction in deep convection, in line with the decrease in deep convective mass transport.

As discussed in Marquet (2017), the isentropic streamfunction may have different characteristics depending on the definition of the equivalent potential temperature, which could impact the robustness of our results that depend on the isentropic streamfunction. Given this, we examined changes with surface drying in the deepest and median trajectories from the isentropic streamfunction, with this streamfunction computed using Marquet (2011)'s entropy potential temperature θ_s (Text S4, Table 1). A minor difference between our main results and those obtained with θ_s is that it is not

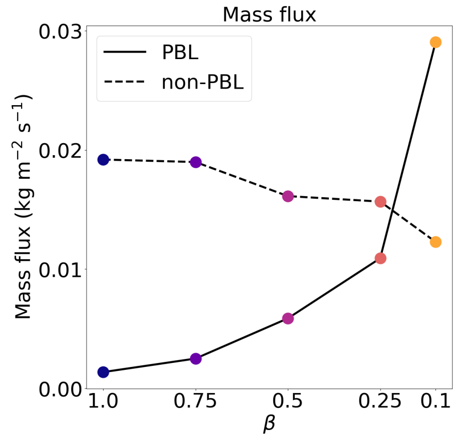

FIG. 5. Mean upward vertical mass flux within the PBL (solid line) and excluding the PBL (dashed line), computed during the 20-day steady-state periods from each simulation, versus β.

clear that the difference in the entropy potential temperature between the updraft and the downdraft decreases under surface drying, with the exception of the driest experiment (Fig. S37). Otherwise, the trends under surface drying discussed in this text are not qualitatively sensitive to the definition of the equivalent potential temperature.

b. Surface Drying Transition in Other Thermodynamic Spaces

Figure 6 presents the response to surface drying of the isentropic streamfunction projected into three thermodynamically-relevant spaces: temperature-entropy (Fig. 6a, b), vapor mixing ratio-vapor Gibbs free energy (Fig. 6c, d), and height-total mixing ratio space (Fig. 6e, f). All quantities are defined as in Régibeau-Rockett et al. (2024). Here, the increase in the total mixing ratio during subsidence (Fig. 6e) is due to mixing of the subsiding air with cloudy air due to convective detrainment, as well as re-evaporation of precipitation in the free troposphere (Pauluis 2016). Note also that the specific Gibbs free energy of water vapor g_v can be approximated as $g_v \approx R_v T \log \mathscr{H}$ (Pauluis 2011). The term g_v is primarily dependent on changes in $\mathscr{H}$ (Pauluis 2016), and is close to zero at saturation and negative/positive for unsaturated/supersaturated air. For example, in the simulation with β=1 (Fig. 6c), the unsaturated near-surface air is represented by the portion of the deep trajectory with $g_v \approx -50$ kJ kg^{-1} and the vapor mixing ratio r_v increasing from roughly 0.015 to 0.016 kg kg^{-1}. The LCL is the point at which air rising upwards from the surface at relatively constant r_v reaches the point past which g_v is close to zero, representing the saturated updraft.

Atmospheric convection involves the removal of water at a higher (near-zero) Gibbs free energy than the value of g_v at which water is added via surface evaporation (Pauluis 2011, 2016). This separation results in irreversible entropy production that reduces the mechanical work output from the atmospheric heat engine (Pauluis 2011, 2016).

The projection of ψ into height-total mixing ratio ($z - r_T$) space (Fig. 6e,f) demonstrates in greater detail the increase in height of the diagnosed LCL—represented by the height at which the range of the total vapor mixing ratio r_T (kg kg^{-1}) increases markedly between the updraft and the downdraft—over the transition. As can be seen in the temperature-entropy plot (Fig. 6b), the temperature at which the entropy range of the circulation experiences a large growth decreases with increased surface drying. This implies that the temperature of the LCL diminishes with decreasing β (Table 1). This is in line with Bolton (1980)'s formula for the temperature of the LCL implied by the temperature dependence of the saturation vapor pressure. The decrease in the temperature and increase in height of the LCL in response to surface drying is confirmed by inspection of the horizontal- and time-mean vertical profiles of temperature in the simulations (Fig. 7). Here, the diagnosed LCL is the point above which the lapse rate becomes less negative with height due to the latent heat released in convective updrafts.

The sharp decrease in the updraft entropy of the deep trajectory above the LCL in temperature-entropy space (Fig. 6a) is likely representative of the exchange of water mass between the updraft and its environment due to convective entrainment and detrainment (Pauluis 2016). In tropical cyclones, the eyewall updraft air experiences a very small decrease in its entropy due to little dry-air entrainment occurring during ascent (Pauluis and Zhang 2017). For our simulations, the decrease in updraft entropy, δs_{up}, is much weaker for lower values of β (Fig. 6b, Table 1), which could represent a decrease in convective entrainment and detrainment. Another possible explanation is that these processes do not substantially change the entropy of the updraft air because of a more uniform atmospheric humidity distribution. Fig. 8 shows the changes in the isentropic-average vapor mixing ratio as the surface dries, together with the deep and median trajectories from the isentropic streamfunction. The humidity gradient between the rising and descending branches of the circulation strongly decreases as β is lowered (Table 1). Because our analysis cannot quantify changes in convective entrainment, it is possible that the entrainment rate also varies under surface drying.

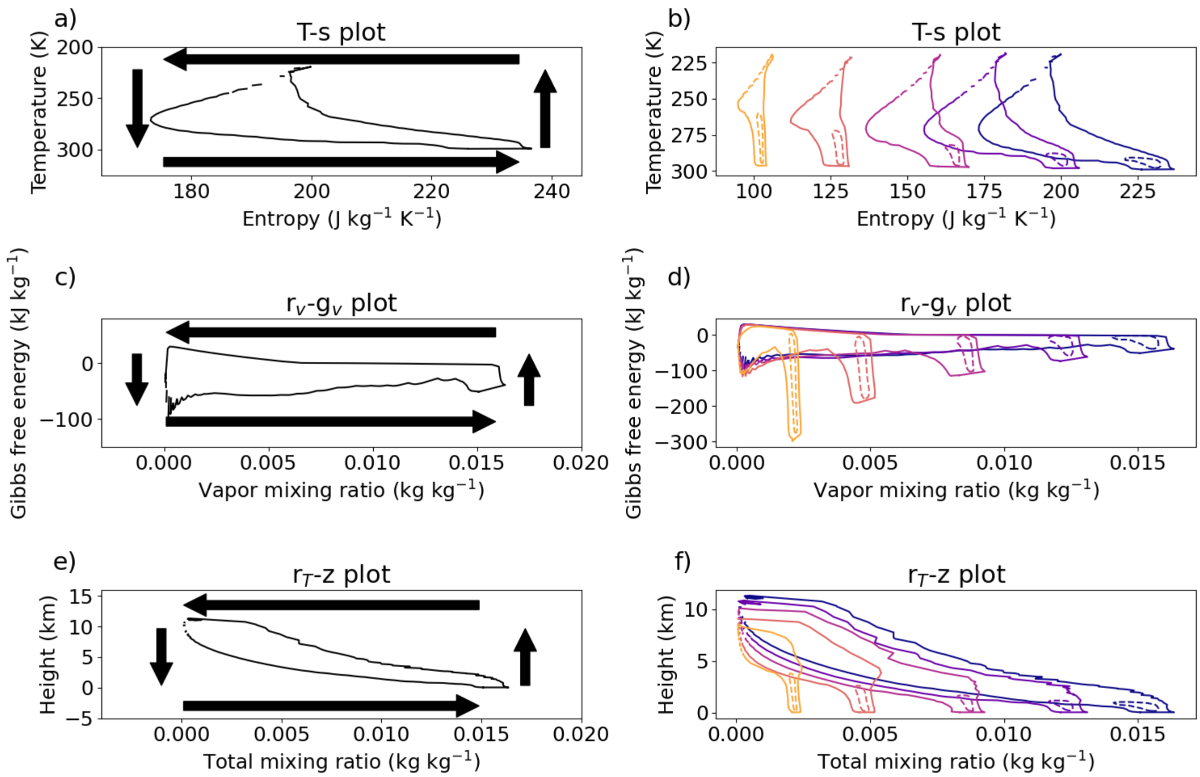

FIG. 6. Left: Isentropic streamfunction, $\psi(z, \theta_e)$, from the β = 1 simulation projected into a) temperature-entropy space, c) vapor mixing ratio-vapor Gibbs free energy space, and e) height-total water mixing ratio space. Black arrows show the direction of the thermally direct overturning circulation. Right: Comparison of the deepest (solid lines) and median (dashed lines) trajectories derived from ψ for each simulation in b) temperature-entropy space, d) vapor mixing ratio-vapor Gibbs free energy space, and f) height-total water mixing ratio space.

The smaller decrease of r_T during the upward branch of the deep trajectory in $z - r_T$ space implies a lower precipitation rate in the drier simulations (Fig. 6f, Table 1). This is confirmed by inspection of the time- and horizontal-average surface precipitation rate in the constant-β simulations (Fig. 9, Table 2), which decreases by 95% from the fully moist simulation to the driest simulation. However, because surface drying also results in a deeper and drier PBL, this does not necessarily imply a reduction in precipitation re-evaporation in the PBL. We examined changes in the mean percentage difference in the relative humidity ($\mathscr{H}_{GG}$)—defined with respect to both ice and liquid water as in Goff and Gratch (1946) and Régibeau-Rockett et al. (2024)—between the PBL portions of the updraft and downdraft branches of the deepest isentropic streamfunction trajectory (Table 1). Here,

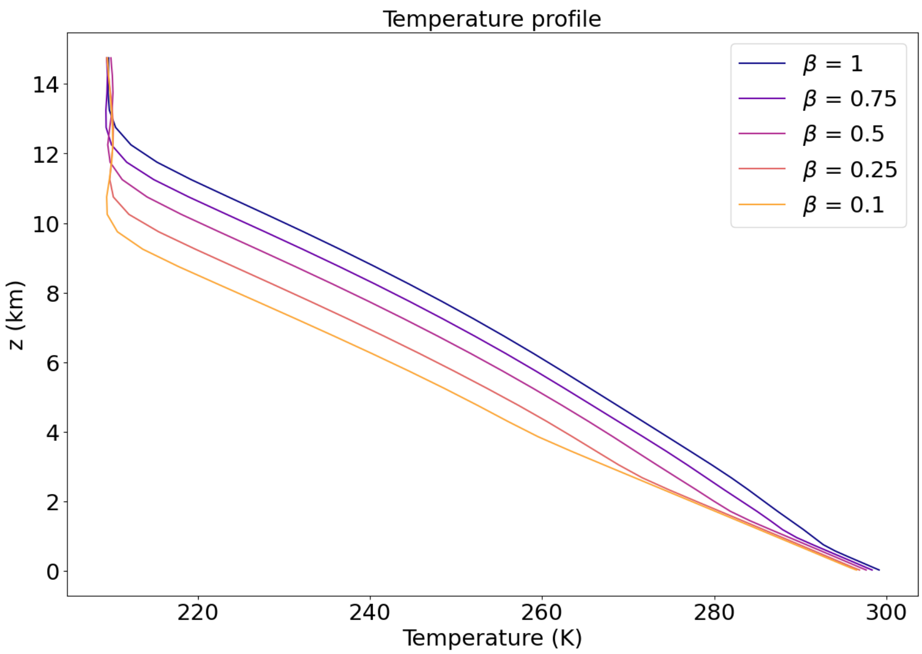

FIG. 7. Time- and horizontal-mean vertical profiles of absolute temperature (K) from the 20-day steady-state periods in each constant-β simulation.

the percent difference is computed with respect to the relative humidity of the downdraft profile. The updraft profile is assumed to represent the PBL below convective clouds while the downdraft profile represents the state of the PBL far from convective updrafts. Elevated re-evaporation of precipitation in the regions near convective clouds should then yield a larger relative humidity difference between the updraft and downdraft profiles. The relative humidity difference increases by 13% from the fully moist simulation to the driest simulation. This is consistent with increased PBL re-evaporation of precipitation under surface drying.

Over the transition from moist to nearly dry, the change in g_v from the surface to the diagnosed LCL becomes much more positive (Fig. 6d, Table 1). This implies that water vapor transport along this pathway is increasingly non-spontaneous under surface drying, consistent with the decrease in above-PBL convective mass transport (Fig. 5, Table 2). Since g_v is close to zero for the saturated updraft, the surface-to-LCL g_v difference grows largely because the value of g_v for near-surface air becomes strongly negative for low β (Fig. 6d, Table 1). Both the near-surface g_v and the irreversible entropy production from surface evaporation (Kleidon 2008) depend on $\log \mathscr{H}_{ns}$, where $\mathscr{H}_{ns}$ is the relative humidity with respect to liquid water near the surface. As the relative humidity

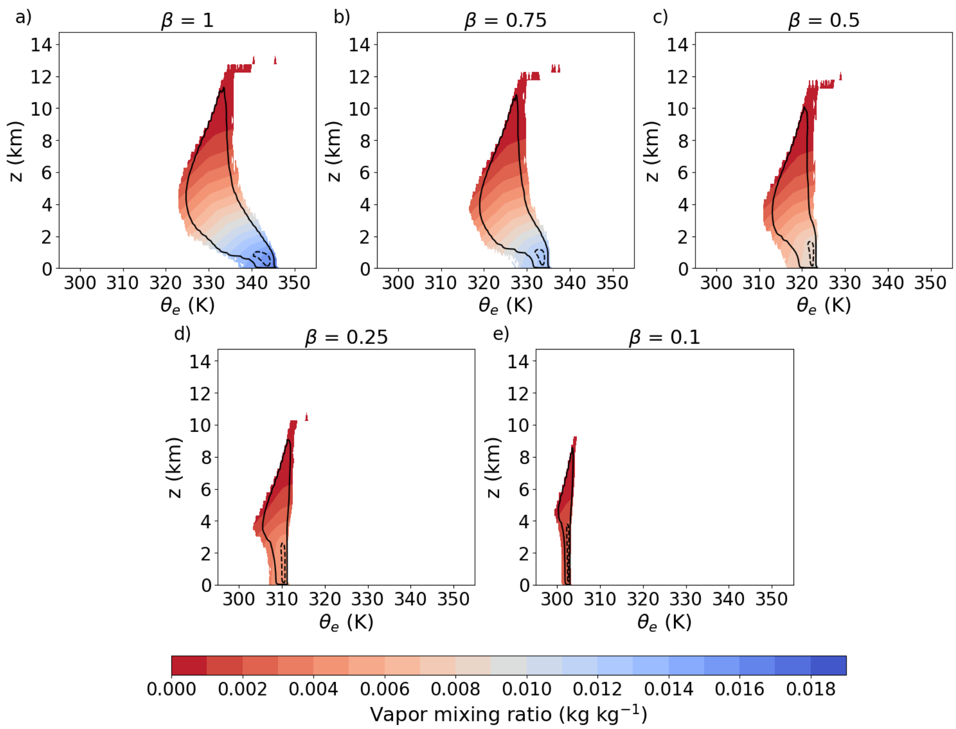

FIG. 8. Comparison of the mass-weighted isentropic-average vapor mixing ratio (colors), and the deepest and median trajectories from ψ for the simulations with β = a) 1, b) 0.75, c) 0.5, d) 0.25, and e) 0.1. All quantities are computed during the 20-day steady-state periods from each simulation.

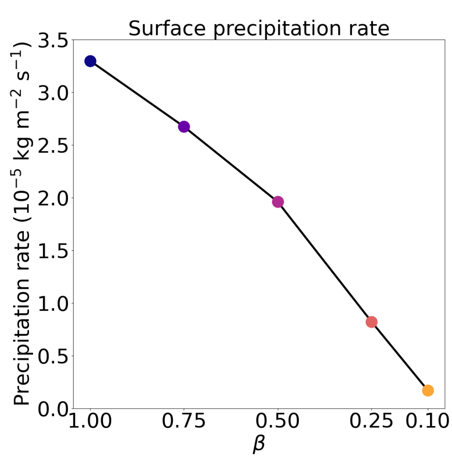

FIG. 9. Time- and horizontal-mean precipitation rate, computed during the 20-day steady-state periods from each simulation, versus β.

of the surface—the source of moisture to the atmosphere—decreases, we hypothesize that the boundary layer becomes much drier and so the irreversibility associated with surface evaporation grows significantly, represented by the increasingly negative value of g_v near the surface.

We test this by examining the variability in the surface irreversible entropy production under surface drying. Evaporation from an unsaturated surface into the atmosphere is associated with an irreversible entropy production (Kleidon 2008):

$$\Delta S_{surf} = -R_v d_v^z \log \frac{\mathscr{H}_{ns}}{\mathscr{H}_s}, \tag{2}$$

where d_v^z is the vertical mass flux of water vapor from the surface to the atmosphere (kg m^{-2} s^{-1}) and $\mathscr{H}_s = \beta$ is the surface relative humidity. Here, we have assumed that the near-surface air is at the same temperature as the surface. We have also corrected a sign error in Kleidon (2008)'s formula for ΔS_{surf} that caused it to differ from a commonly-used expression for ΔS_{surf} that assumes a saturated surface (Pauluis and Held 2002a,b). The term $\mathscr{H}_{ns}$ is approximated using the mean value of $\mathscr{H}_{GG}$ in the portion of the deep trajectory that intersects with the lowest model level. As shown in Table 1, the irreversible entropy production from surface evaporation decreases under surface drying, becoming close to zero for the driest experiments. This is because although the relative humidity of the boundary layer decreases under surface drying, it does not dry as quickly as the surface and so $\frac{\mathscr{H}_{ns}}{\mathscr{H}_s}$ increases. Combined with the reduction in d_v^z inferred from the lower latent heat flux (Fig, 4, Table 2), this leads to ΔS_{surf} decreasing to close to zero under very dry conditions.

Figure 10 and Table 1 show changes in the g_v difference due to surface evaporation, $\Delta g_{v,s}$, under surface drying:

$$\Delta g_{v,s} = g_{v,ns} - g_{v,s},$$
$$g_{v,s} = R_v T_s \log \mathscr{H}_s + c_{p,l}(T_s - T_{ref} - T_s \log \frac{T_s}{T_{ref}}).$$

Here, $g_{v,ns}$ (J kg^{-1}) is the mean near-surface value of g_v in the portion of the deep trajectory that intersects with the lowest model level and $g_{v,s}$ (J kg^{-1}) is the surface vapor Gibbs free energy. In the moister simulations, $\Delta g_{v,s}$ is negative, while it becomes positive under drying. For high values of β, near-surface air is drier than the surface and surface evaporation occurs spontaneously, whereas in our drier simulations the near-surface air is more humid than the surface and surface evaporation is non-spontaneous.

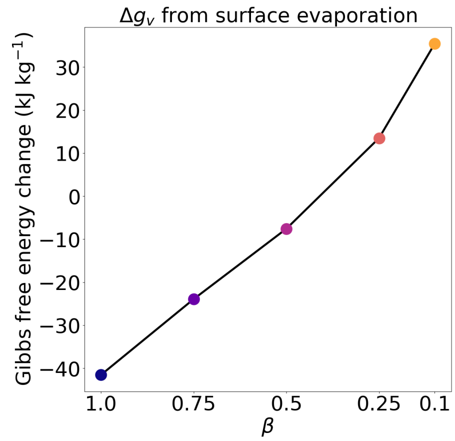

FIG. 10. Change in specific water vapor Gibbs free energy due to surface evaporation ($\Delta g_{v,s}$), computed during the 20-day steady-state periods from each simulation, versus β.

Finally, comparison of the deep trajectories in Fig. 6b reveals that although under surface drying the atmospheric circulation becomes shallower in terms of its maximum height, the lowest temperature experienced by the deep circulation remains close to steady as β lowers (Table 1). This is consistent with a decrease in the tropopause height in the drier simulations, which is confirmed to occur by inspection of the mean vertical profiles of temperature (Fig. 7, Table 2). Importantly, the former result is strongly sensitive to both the microphysics and PBL schemes (Text S2, S3, Table 1), as will be discussed in the next section.

4. Discussion

a. Convective mass transport and energetics

The growth in the overall convective mass transport that we observe as the surface dries is in line with the findings of previous CPM studies of disorganized oceanic RCE convection (Pauluis 2000; Pauluis and Held 2002a; Singh and O'Neill 2022). Pauluis and Held (2002a) compare moist and dry RCE simulations, finding that convective updrafts are more ubiquitous in dry RCE compared to moist RCE. The same qualitative result was observed by Singh and O'Neill (2022) at a height of 4 km. Pauluis (2000)'s drier simulations also show widespread and stronger updrafts compared to moister simulations. This could correspond to a larger overall convective mass transport. Pauluis and Held (2002a) additionally find that the turbulent dissipation of kinetic energy—which in a steady state is equal to the rate of kinetic energy work associated with convective motions—is much larger in dry RCE than in moist RCE, in line with the strong increase in the mean dissipation rate under drying in our simulations (not shown). This metric is strongly related to the mass transport by convection, and so this finding agrees with the larger convective mass transport that we find in our drier simulations.

However, our results are qualitatively different from those of previous studies investigating the impacts of atmospheric drying on tropical cyclones. Alland et al. (2017) find that the convective mass transport by the tropical cyclone eyewall updraft decreases as the initial amount of moisture above the LCL decreases over their suite of simulation ensembles. Meanwhile, Mrowiec et al. (2011) and Cronin and Chavas (2019) both observe decreases in the eyewall updraft velocity in dry tropical cyclones compared to moist simulations of these storms. The contrast between the response of tropical cyclone updrafts and localized convective updrafts to atmospheric drying may represent a difference in the response of tropical cyclones, which are highly organized convective systems, to changes in atmospheric moisture compared to the response of disorganized convection. It is possible that the behavior of other organized convective systems, such as mesoscale convective systems or extratropical cyclones, may follow more closely the response of tropical cyclones to surface drying than the changing behavior of disorganized convection that we observe. A study comparing the impacts of surface drying on organized convective systems to the response of disorganized convection to the same change has not been attempted to date.

We next compare our results to those of large-scale moist-to-dry studies. Mitchell et al. (2009) investigate the response of the Hadley Cell to a combination of surface drying and a reduction in the relative humidity threshold for convection. They find that the Hadley Cell is more intense in drier conditions, which may imply an increased mass transport, in line with our results. However, McKinney et al. (2022) observe that the Hadley Cell's intensity does not significantly change in response to surface drying. The authors also investigate the effect of a reduced atmospheric saturation vapor pressure on the Hadley Cell, finding in this case that its intensity is weaker under drier conditions. The discrepancy between these results could imply a dependence of the change in the mass transport on the form of applied atmospheric drying, as will be discussed in section 5.

In our simulations, the overall increase in the convective mass transport under drying is primarily due to a strong increase in the mass transport by PBL convection, whereas the convective mass transport above the PBL is lower in drier conditions. The latter is consistent with van der Drift and O'Gorman (2025)'s oceanic study. The authors investigate changes in disorganized convection under an increased vegetative evaporative resistance. A higher surface temperature is imposed for drier conditions to hold the free-tropospheric temperature constant. The authors find that the average convective mass transport decreases under drying for atmospheric columns surpassing the 99.9th percentile of the column-integrated condensation rate. This extreme precipitation rate should be associated with deep convection. The imposed increase in the surface temperature accompanying drying complicates a direct comparison between this study and ours. However, the authors' results are consistent with the decrease in deep convective mass transport that we observe in response to surface drying.

In this work, the increase in the convective mass transport occurs despite a reduction in the total convective heat transport implied by the decreases we observe in the total surface heat flux and net radiative cooling at lower β values. A decrease in the total surface heat flux is observed in dry RCE compared to moist RCE by both Pauluis and Held (2002a) and Singh and O'Neill (2022). McColl and Tang (2024)'s terrestrial RCE study also demonstrates that column radiative cooling is lower under surface drying. Additionally, Wang and Lin (2021) find that dry tropical cyclones experience less radiative cooling than moist tropical cyclones. Pauluis (2000) investigates these changes in greater detail and observes a gradual decrease in the atmospheric net radiative heat loss over a suite of moist-to-dry RCE simulations, although it should be noted that the author employs a simpler Newtonian cooling scheme for radiation compared to our fully interactive radiative scheme.

b. Vertical structure of the circulation

In our experiments, surface drying results in a deepening of the PBL. This finding is in line with results of previous observational studies, which generally find that the daily-maximum height of the PBL is largest over drier regions, such as Australia, the Sahara, and the western United States (Seidel et al. 2012; von Engeln and Teixeira 2013; Zhang et al. 2020). This result is additionally consistent with the study of Wang and Lin (2020), who find that dry tropical cyclones have a deeper inflow layer compared to moist tropical cyclones. Because tropical cyclone inflow occurs in the tropical cyclone boundary layer, this implies that this layer is deeper in their dry experiment than under moist conditions. The deepening of the PBL is also supported by several moist-to-dry studies over ocean lower boundaries (Zsom et al. 2012; Fan et al. 2021; Spaulding-Astudillo and Mitchell

2023; van der Drift and O'Gorman 2025). For example, in the 1-D cloud model investigation of Zsom et al. (2012) the authors find, using an Earth-like configuration of their model, that a lower atmospheric relative humidity causes liquid water clouds to form at higher elevations, implying a deeper PBL. Spaulding-Astudillo and Mitchell (2023) also observe a deepening of the PBL in response to atmospheric drying, accompanied by a higher LCL. In our simulations, the PBL deepens under surface drying because the LCL is higher. The temperature-dependent constraint on the mass fraction of atmospheric water vapor (Bolton 1980) predicts that the LCL will be cooler and therefore higher in a drier atmosphere. This is in line with the lower LCL temperature in our drier simulations. A similar explanation is briefly provided by Seidel et al. (2012) to explain the deeper PBLs they identify in the drier U.S. compared to Europe.

We also find that the simulations with lower β values have lower tropopause heights. Cronin and Chavas (2019) find an increase of the pressure of the tropopause with surface drying in their moist-to-dry simulations, although this does not necessarily imply a decrease in the tropopause height. Similarly, Spaulding-Astudillo and Mitchell (2023) observe that the height above which the magnitude of the atmospheric lapse rate significantly decreases is lower in their drier experiments, implying a reduced tropopause height. A lower tropopause in dry compared to moist RCE is observed by Singh and O'Neill (2022) in their simulations of localized convection. Specifically, the authors find that the tropopause is roughly 5 km lower in their dry simulation compared to the moist simulation. Assuming a linear scaling of the tropopause height with surface drying, this would correspond to a decrease of 4.5 km from fully moist conditions to those corresponding to our simulation with $\beta = 0.1$. In comparison, the height of the lapse-rate tropopause (WMO 1957) in our simulations, computed as in Xian and Homeyer (2019), decreases by 2.5 km between the fully moist and driest simulations (Table 2). This is substantially less than the estimated decrease given the results of Singh and O'Neill (2022). This may indicate that most of the transition towards a fully dry temperature lapse rate—and an associated decrease in the tropopause—chiefly occurs at low values of atmospheric moisture below the range studied here. It is also possible that this results from the differences in the construction of Singh and O'Neill (2022)'s moist and dry simulations compared to our surface relative humidity scaling. Finally, we note that Pauluis (2000) does not observe a consistently-signed change in the height of the tropopause with atmospheric drying: for experiments in which the whole atmosphere's specific humidity is reduced to 50% and 5% of its fully moist value, respectively, the tropopause height decreases as the atmosphere dries, in line with our results. However, when the specific humidity is further reduced from 5% to 0.5% of its fully moist value, the tropopause height increases as the atmosphere becomes drier. The lowest value of β examined in our simulations is above the range at which Pauluis (2000) observes a reversal in the tropopause height's response to surface drying. It is possible that we would find non-monotonicity in our simulations if we examined lower β values.

The deepening PBL combined with the lower tropopause result in much shallower atmospheric convection in our drier experiments. This is consistent with the shallower convection found in dry RCE compared to moist RCE by Pauluis and Held (2002a) and Singh and O'Neill (2022). Several studies of the moist-to-dry transition also observe that atmospheric convection becomes shallower in drier conditions (Mitchell et al. 2006; McKinney et al. 2022; Spaulding-Astudillo and Mitchell 2023). Additionally, Mrowiec et al. (2011) and Cronin and Chavas (2019) find that the overturning circulation of simulated tropical cyclones is shallower in dry or near-dry RCE than in moist RCE.

Although the precipitation rate decreases under surface drying in our simulations, our results are consistent with more re-evaporation of precipitation in the PBL under surface drying, in line with the results of van der Drift and O'Gorman (2025)'s oceanic study. As discussed by the authors, the inferred larger re-evaporation of precipitation in our simulations likely occurs because it falls through a much deeper and drier PBL in the experiments with lower β values. The authors additionally find substantial decreases in the precipitation efficiency under drying due to the increased re-evaporation, which likely also occurs in our simulations.

c. Convective-top temperature

For our main suite of simulations, a projection of the isentropic streamfunction into temperature-entropy space reveals that the lowest temperature achieved by the deepest convective trajectories is nearly invariant with surface drying, although this result is not robust across our sensitivity tests as we discuss below (Table 1). Because the minimum temperature of convective clouds typically occurs at the cloud top, this implies that the diagnosed cloud top temperature is close to constant with varying surface moisture in our main suite of simulations. Hartmann and Larson (2002) introduced the Fixed Anvil Temperature (FAT) hypothesis, which argues that the temperature of tropical cloud anvils remains fixed regardless of the surface temperature. Although some studies have challenged the existence of FAT and proposed alternatives (e.g. Zelinka and Hartmann 2010; Igel et al. 2014; Seeley et al. 2019), several numerical modeling and observational studies have supported FAT (e.g. Xu et al. 2005; Kuang and Hartmann 2007; Eitzen et al. 2009; Khairoutdinov and Emanuel 2013; Singh and O'Gorman 2015), and the hypothesis has been extended from the context of the tropics to the global atmosphere (Thompson et al. 2017). Although the FAT hypothesis was developed for the context of an atmosphere under an increasing surface temperature, its arguments may be applicable to cloud anvil temperature variability under varying surface moisture. This is because the main arguments of FAT are based on the following (Hartmann and Larson 2002):

- The Clausius-Clapeyron relation places a temperature-dependent constraint on atmospheric moisture content.
- Clear-sky radiative cooling in the troposphere is dominated by longwave emission from water vapor.
- A maximum decrease of clear-sky radiative cooling with height (occurring at around the level where the atmospheric water vapor content becomes negligible, assuming the first and second listed points are valid) creates a maximum in clear-sky convergence, which must be balanced by strong convective divergence.

The first and third statements above should hold regardless of the total amount of moisture at the surface and in the atmosphere itself. The second argument may not be valid in an atmosphere with sufficiently low water vapor, or in one in which constituents other than water vapor make major contributions to radiative cooling. An extension of FAT to the context of varying surface moisture has not previously been investigated in detail, and requires detailed radiative analysis that is beyond the scope of the present study. Future works should investigate whether the FAT hypothesis might be extended to situations besides varying surface temperature, such as varying surface moisture.

Although the diagnosed convective top temperature is close to constant as the surface dries in the main suite of simulations, this result is not robust to the choice of microphysics or PBL scheme (Text S2, S3). Although the diagnosed convective top temperature is also nearly invariant in the Thompson suite, in all other sensitivity tests the lowest temperature sampled by the deep trajectories increases by up to 7 K from the fully moist to the driest simulations. The latter is qualitatively in line with the increase in the temperature of the convective top in response to decreased atmospheric relative humidity found by Thuburn and Craig (2002) in their simple radiative-convective model without explicit convection. Spaulding-Astudillo and Mitchell (2023) also observe that the temperature at the peak high cloud fraction increases under atmospheric drying.

5. Conclusions

In this work, we investigated the changing characteristics of moist convection subjected to surface drying from the thermodynamic perspective of the convective isentropic streamfunction. Our findings are as follows: as the surface dries, the separation in the entropy of convective updraft air and downwelling air decreases (Fig. 2, Table 1). This is accompanied by an increase in the isentropic mass transport—which is related to the overall convective mass transport—and a deepening of the PBL (Figs. 2, 3 and 6f, Table 1). The increase in the isentropic mass transport is mainly due to a strong increase in PBL convective mass transport, whereas the mass transport by deep convection decreases in response to drying (Fig. 5, Table 2) due to a reduction in CAPE and an increase in CIN (Table 2). Meanwhile, the total heating and cooling of the atmosphere, represented by the surface total heat fluxes and domain-integrated net radiative cooling, decrease as the parameter β decreases (Fig. 4, Table 2), implying a reduction in the heat transport by convection. The convective heat transport is dependent on both the mass transport by convection and the difference in equivalent potential temperature between the updraft and downdraft. Although the isentropic mass transport increases in drier conditions, this does not contradict the inferred decrease in the convective heat transport because there is a strong reduction in the updraft/downdraft equivalent potential temperature difference under surface drying.

Further insight into the response of convection to surface drying is gained by projecting the isentropic streamfunction into various thermodynamic spaces (Fig. 6, Table 1, Table 2), such as temperature-entropy space (Fig. 6a,b). The weakening gradient of entropy along the updraft of the deepest trajectories of the isentropic streamfunction in the drier simulations is consistent with a smaller thermodynamic signature of exchange with the environment due to entrainment and detrainment. This partially results from a decreasing gradient of water vapor between the updraft and its surroundings. However, our analysis cannot determine whether entrainment and detrainment rates change under surface drying. Also, our results are inconclusive regarding the response of the diagnosed cloud top temperature to surface drying, since this response is strongly dependent on the choice of PBL and microphysics schemes. While in two simulation suites the diagnosed convective top temperature is nearly invariant under drying, it instead increases in all other sensitivity suites. Additionally, computation of the relative humidity and vapor Gibbs free energy in the near-surface branch of the isentropic streamfunction demonstrates that under surface drying, surface evaporation is associated with less irreversible entropy production and transitions from a spontaneous process to a non-spontaneous process. This is because near-surface air is drier than the surface when the latter is closer to saturation but is more humid than the surface under drier conditions. Other findings of this work include that surface drying results in a reduced precipitation rate, an inferred increase in re-evaporation of precipitation in the PBL, a reduction in the temperature of the LCL, shallower convection, and a lower tropopause.

This work includes several idealizations that may limit the applicability of our findings to real atmospheric convection. First, our simulations are conducted over an oceanic lower boundary. Although the drying of this lower boundary may still capture some of the convective changes resulting from atmospheric drying over land, there are many important differences between land and ocean lower boundary conditions, even in highly idealized models. Future work should verify whether the convective changes in response to atmospheric drying observed here are generalizable to atmospheres over land. Second, the behavior of convection in response to atmospheric drying discussed here may depend on the surface layer parameterization employed in our study. Future work should verify whether our results are robust under alternative surface schemes. Additionally, the simulations analyzed here are designed based on the characteristics of Earth's current atmosphere. Although it is possible that our results could be generalized to the atmospheres of other planets with significant amounts of atmospheric water vapor or another condensable component, ensuing studies should verify whether our findings hold when the similarity of the simulated atmosphere to Earth's is relaxed.

Our simulations were conducted in a small domain to prevent convective self-aggregation from occurring. We chose to exclude self-aggregated convection from our analysis because organized convective systems such as self-aggregated convection may respond quite differently to surface drying than disorganized convection. Compared to disorganized convection, convective updrafts in aggregated systems are more shielded, on average, from mixing with the drier non-convecting environment because the near-plume environment is moister (e.g. Grabowski and Moncrieff 2004; Tompkins and Semie 2017; Becker et al. 2018). As such, the effects of atmospheric drying may have less of an impact on organized convection compared to disorganized convection. Aggregated convection also contains fewer high clouds and more low clouds than disorganized convection (e.g. Tobin et al. 2012; Wing and Cronin 2016; Bony et al. 2016). Hence, the response of aggregated convective systems to imposed drying may be more weighted towards changes in low clouds than deep convective clouds. Finally, the degree of convective self-aggregation may vary under surface drying. All these factors could complicate the interpretation of our results. This small-domain study allowed us to examine the fundamental convective response to surface drying. However, our results may not apply to organized convective systems or large-domain RCE, which supports convective self-aggregation. Indeed, some of our results differ from the findings of moist-to-dry studies of tropical cyclones—highly organized systems—although the majority are consistent with them. Future work should examine the response of organized convection, such as self-aggregated convection, to changes in atmospheric moisture content.

We investigated the effects of atmospheric drying on convection through drying the surface and allowing our simulations to come to a new, statistically steady RCE state. However, other methodologies of atmospheric drying have been employed in the literature, such as reducing the atmospheric saturation vapor pressure by a constant everywhere (Pauluis 2000; McKinney et al. 2022; Spaulding-Astudillo and Mitchell 2023; McKinney and Mitchell 2024). It is possible that our results are sensitive to the form of the applied atmospheric drying. As discussed herein, many of our results are supported by the findings of moist-to-dry studies that employed different drying methodologies (Pauluis 2000; Zsom et al. 2012; Spaulding-Astudillo and Mitchell 2023). For example, the results of both Spaulding-Astudillo and Mitchell (2023) and Pauluis (2000) are broadly in agreement with ours, and are derived from suites of simulations in which the atmospheric saturation vapor pressure was varied. As noted previously, two studies of the Hadley circulation under drying disagree on how the Hadley cell's intensity, which relates to the mass transport, changes in drier conditions (Mitchell et al. 2009; McKinney et al. 2022). The sign and magnitude of this change vary across the three different atmospheric drying methods employed in these studies. This implies that the increase in convective mass transport that we observe may be sensitive to the atmospheric drying approach. On the other hand, our result is in line with the findings of Pauluis

(2000), who uses a different drying method compared to our study, implying that our findings may not be sensitive to the form of the applied drying. It is possible that the Hadley cell's response to drying is more sensitive to the drying method compared to localized convection. However, the degree to which the mass-transport response of localized convection depends on the drying methodology remains uncertain and should be examined in future work.

Acknowledgments. We are grateful to Olivier Pauluis, Noah Diffenbaugh, Leif Thomas, Aditi Sheshadri, and Jonathan Mitchell for their helpful feedback on this manuscript. We are also thankful to the Stanford Research Computing Center staff for their technical support during this project, and for allowing us to carry out this study via the use of their high-performance computing cluster. We are additionally grateful to George Bryan for creating and maintaining the CM1 model code for the community. Some portions of this paper are published in thesis form in fulfillment of the requirements for the Ph.D. (Régibeau-Rockett 2025).

Data availability statement. All simulations were run using the Cloud Model 1, version 21.1, which is available at `https://www2.mmm.ucar.edu/people/bryan/cm1/`. Modified model source code, as well as input and output files, is available at `https://doi.org/10.5281/zenodo.17352676`. Finally, our analysis code is located at `https://doi.org/10.5281/zenodo.17352687`.

APPENDIX

Computation of the energy budget

In a simulated RCE atmosphere, the total energy of the atmosphere is statistically steady and conservation of energy requires that:

$$\overline{LHF} + \overline{SHF} + [Q_{rad}] = 0, \tag{A1}$$

where $\overline{X}$ denotes the time- and horizontal-mean value of X, and $[X]$ is equal to the time-average, domain-integrated value of X divided by the area of the surface. The terms LHF and SHF (W m^{-2}) are the bulk surface fluxes of latent and sensible heat, repectively, and Q_{rad} (W m^{-3}) is the radiative heating rate per unit volume. The LHF is defined as in Eq. (1), and the SHF is computed in the model as (Jiménez et al. 2012):

$$SHF = \rho_1 c_{p,d} C_h U(\theta_s - \theta_1).$$

Here, $c_{p,d}$ (J kg^{-1} K^{-1}) is the specific heat capacity of dry air at constant pressure, C_h is a dimensionless bulk transfer coefficient, and θ_s and θ_1 are, respectively, the potential temperature (K) at the surface and at the lowest model level.

The first law of thermodynamics under moist, constant-volume conditions states that:

$$dQ = \rho c_{v,m} dT, \tag{A2}$$

where ρ (kg m^{-3}) is the dry-air density and $c_{v,m}$ (J kg^{-1} K^{-1}) is the heat capacity of humid air under constant-volume conditions, defined as in CM1:

$$c_{v,m} = c_{v,d} + c_{v,v} r_v + c_{p,l} r_l + c_{p,fr} r_{fr}.$$

Here, $c_{v,d}$ (J kg^{-1} K^{-1}) is the heat capacity of dry air under constant-volume conditions, $c_{v,v}$ (J kg^{-1} K^{-1}) is the heat capacity at constant volume of water vapor, and $c_{p,l}$ and $c_{p,fr}$ are the heat capacities of liquid and solid water under constant-pressure conditions (J kg^{-1} K^{-1}). The terms r_v, r_l, and r_{fr} are the mixing ratios of water vapor, liquid water, and solid water (kg kg^{-1}).

In accordance with Eq. (A2), Q_{rad} is computed from the model-output time tendencies of temperature due to the longwave and shortwave forcings in the radiative scheme, $\dot{T}_{rad,SW}$ and $\dot{T}_{rad,LW}$, as:

$$Q_{rad} = \rho c_{v,m} (\dot{T}_{rad,SW} + \dot{T}_{rad,LW}). \tag{A3}$$

References

Alland, J. J., B. H. Tang, and K. L. Corboseiro, 2017: Effects of Midlevel Dry Air on Development of the Axisymmetric Tropical Cyclone Secondary Circulation. *J. Atmos. Sci.*, **74**, 1455–1470, https://doi.org/10.1175/JAS-D-16-0271.1.

Barth, E. L., and S. C. R. Rafkin, 2007: TRAMS: A new dynamic cloud model for Titan's methane clouds. *Geophys. Res. Lett.*, **34**, L03 203, https://doi.org/10.1029/2006GL028652.

Becker, T., C. S. Bretherton, C. Hohenegger, and B. Stevens, 2018: Estimating bulk entrainment with unaggregated and aggregated convection. *Geophys. Res. Lett.*, **45**, 455–462, https://doi.org/

10.1002/2017GL076640.

Beljaars, A. C. M., 1995: The parametrization of surface fluxes in large-scale models under free convection. *Quart. J. Roy. Meteor. Soc.*, **121**, 255–270, https://doi.org/10.1002/qj.49712152203.

Benneke, B., and Coauthors, 2019: Water Vapor and Clouds on the Habitable-zone Sub-Neptune Exoplanet K2-18b. *The Astrophysical Journal Letters*, **887**, L14, https://doi.org/10.3847/2041-8213/ab59dc.

Benneke, B., and Coauthors, 2024: JWST Reveals CH4, CO2, and H2O in a Metal-rich Miscible Atmosphere on a Two-Earth-Radius Exoplanet. *arXiv astro-ph.EP 2403.03325 [Preprint]*, URL https://arxiv.org/abs/2403.03325.

Bolton, D., 1980: The Computation of Equivalent Potential Temperature. *Mon. Wea. Rev.*, **108**, 1046–1053, https://doi.org/10.1175/1520-0493(1980)108⟨1046:TCOEPT⟩2.0.CO;2.

Bony, S., B. Stevens, D. Coppin, T. Becker, K. Reed, A. Voigt, and B. Medeiros, 2016: Thermodynamic control of anvil cloud amount. *Proc. Natl. Acad. Sci. (USA)*, **113**, 8927–8932, https://doi.org/10.1073/pnas.1601472113.

Bretherton, C. S., P. N. Blossey, and M. Khairoutdinov, 2005: An Energy-Balance Analysis of Deep Convective Self-Aggregation above Uniform SST. *J. Atmos. Sci.*, **62**, 4273–4292, https://doi.org/10.1175/JAS3614.1.

Bryan, G. H., 2008: On the Computation of Pseudoadiabatic Entropy and Equivalent Potential Temperature. *Mon. Wea. Rev.*, **136**, 5239–5245, https://doi.org/10.1175/2008MWR2593.1.

Bryan, G. H., and J. M. Fritsch, 2002: A Benchmark Simulation for Moist Nonhydrostatic Numerical Models. *Mon. Wea. Rev.*, **130**, 2917–2928, https://doi.org/10.1175/1520-0493(2002)130⟨2917:ABSFMN⟩2.0.CO;2.

Bryan, G. H., and R. Rotunno, 2009: The Maximum Intensity of Tropical Cyclones in Axisymmetric Numerical Model Simulations. *Mon. Wea. Rev.*, **137**, 1770–1789, https://doi.org/10.1175/2008MWR2709.1.

Cadieux, C., and Coauthors, 2022: TOI-1452 b: SPIRou and TESS Reveal a Super-Earth in a Temperate Orbit Transiting an M4 Dwarf. *The Astrophysical Journal*, **164**, 96, https://doi.org/10.3847/1538-3881/ac7cea.

Cadieux, C., and Coauthors, 2024: New Mass and Radius Constraints on the LHS 1140 planets: LHS 1140 b Is either a Temperate Mini-Neptune or a Water World. *The Astrophysical Journal Letters*, **960**, L3, https://doi.org/10.3847/2041-8213/ad1691.

Changeat, Q., B. Edwards, A. F. Al-Refaie, A. Tsiaras, I. P. Waldmann, and G. Tinetti, 2019: Disentangling atmospheric compositions of K2-18 b with next generation facilities. *Exp. Astron.*, **53**, 391–416, https://doi.org/10.1007/s10686-021-09794-w.

Cronin, T. W., and D. R. Chavas, 2019: Dry and Semidry Tropical Cyclones. *J. Atmos. Sci.*, **76**, 2193–2212, https://doi.org/10.1175/JAS-D-18-0357.1.

Dauhut, T., J.-P. Chaboureau, P. Mascart, and O. Pauluis, 2017: The Atmospheric Overturning Induced by Hector the Convector. *J. Atmos. Sci.*, **74**, 3271–3284, https://doi.org/10.1175/JAS-D-17-0035.1.

Ding, F., and R. T. Pierrehumbert, 2016: Convection in Condensible-Rich Atmospheres. *The Astrophysical Journal*, **822**, 24, https://doi.org/10.3847/0004-637X/822/1/24.

Dunion, J. P., 2011: Rewriting the Climatology of the Tropical North Atlantic and Caribbean Sea Atmosphere. *J. Climate*, **24**, 893–908, https://doi.org/10.1175/2010JCLI3496.1.

Eitzen, Z. A., K. Xu, and T. Wong, 2009: Cloud and Radiative Characteristics of Tropical Deep Convective Systems in Extended Cloud Objects from CERES Observations. *J. Climate*, **22**, 5983–6000, https://doi.org/10.1175/2009JCLI3038.1.

Emanuel, K. A., and M. Bister, 1996: Moist convective velocity and buoyancy scales. *J. Atmos. Sci.*, **53**, 3276–3285, https://doi.org/10.1175/1520-0469(1996)053⟨3276:MCVABS⟩2.0.CO;2.

Evans, D. A., N. J. Beukes, and J. L. Kirschvink, 1997: Low-latitude glaciation in the Palaeoproterozoic era. *Nature*, **386**, 262–266, https://doi.org/10.1038/386262a0.

Fan, B., Z. Tan, T. A. Shaw, and E. S. Kite, 2021: Reducing Surface Wetness Leads to Tropical Hydrological Cycle Regime Transition. *Geophys. Res. Lett.*, **48**, e2020GL090 746, https://doi.org/10.1029/2020GL090746.

Fang, J., O. Pauluis, and F. Zhang, 2019: The Thermodynamic Cycles and Associated Energetics of Hurricane Edouard (2014) during Its Intensification. *J. Atmos. Sci.*, **76**, 1769–1784, https://doi.org/10.1175/JAS-D-18-0221.1.

Goff, J. A., and S. Gratch, 1946: Low-pressure properties of water from -160 to 212 f, in Transactions of the American Society of Heating and Ventilating Engineers, presented at the 52nd annual meeting of the American Society of Heating and Ventilating Engineers. 95–122.

Grabowski, W. W., and M. W. Moncrieff, 2004: Moisture–convection feedback in the tropics. *Quart. J. Roy. Meteor. Soc.*, **130**, 3081–3104, https://doi.org/10.1256/qj.03.135.

Grell, G. A., J. Dudhia, and D. R. Stauffer, 1994: A description of the fifth-generation Penn State/NCAR Mesoscale Model (MM5). Tech. rep., NCAR Tech. Note NCAR TN-398-1-STR.

Hartmann, D. L., and K. Larson, 2002: An important constraint on tropical cloud - climate feedback. *Geophys. Res. Lett.*, **29**, 1951, https://doi.org/10.1029/2002GL015835.

Hoffman, P. F., A. J. Kaufman, G. P. Halverson, and D. P. Schrag, 1998: A Neoproterozoic Snowball Earth. *Science*, **281**, 1342–1346, https://doi.org/10.1126/science.281.5381.1342.

Hong, S.-Y., Y. Noh, and J. Dudhia, 2006: A New Vertical Diffusion Package with an Explicit Treatment of Entrainment Processes. *Mon. Wea. Rev.*, **134**, 2318–2341, https://doi.org/10.1175/MWR3199.1.

Hong, S.-Y., and H. Pan, 1996: Nonlocal Boundary Layer Vertical Diffusion in a Medium-Range Forecast Model. *Mon. Wea. Rev.*, **124**, 2322–2339, https://doi.org/10.1175/1520-0493(1996)124⟨2322:NBLVDI⟩2.0.CO;2.

Hueso, R., and A. Sánchez-Lavega, 2006: Methane storms on Saturn's moon Titan. *Nature*, **442**, 428–431, https://doi.org/10.1038/nature04933.

Igel, M. R., A. J. Drager, and S. C. van den Heever, 2014: A CloudSat cloud object partitioning technique and assessment and integration of deep convective anvil sensitivities to sea surface temperature. *J. Geophys. Res. Atmos.*, **119**, 10 515–10 535, https://doi.org/10.1002/2014JD021717.

Jeevanjee, N., and D. M. Romps, 2013: Convective self-aggregation, cold pools, and domain size. *Geophys. Res. Lett.*, **40**, 994–998, https://doi.org/10.1002/grl.50204.

Jiménez, P. A., J. Dudhia, J. F. González-Rouco, J. Navarro, J. P. Montávez, and E. García-Bustamante, 2012: A Revised Scheme for the WRF Surface Layer Formulation. *Mon. Wea. Rev.*, **140**, 898–918, https://doi.org/10.1175/MWR-D-11-00056.1.

Kasting, J. F., 1988: Runaway and moist greenhouse atmospheres and the evolution of Earth and Venus. *Icarus*, **74**, 472–494, https://doi.org/10.1016/0019-1035(88)90116-9.

Khairoutdinov, M. F., and K. A. Emanuel, 2013: Rotating radiative-convective equilibrium simulated by a cloud-resolving model. *Journal of Advances in Modeling Earth Systems*, **5**, 816–825, https://doi.org/10.1002/2013MS000253.

Kirschvink, J. L., 1992: *Late Proterozoic low-latitude global glaciation: the snowball Earth. In: The Proterozoic biosphere: A multidisciplinary study [Schopf, J. and C. Klein (eds.)]*, 51–52. Cambridge University Press, Cambridge, United Kingdom and New York, NY, USA, https://doi.org/10.1017/CBO9780511601064.

Kleidon, A., 2008: Entropy production by evapotranspiration and its geographic variation. *Soil and Water Research*, **3**, S89–S94, https://doi.org/10.17221/1192-SWR.

Kuang, Z., and D. L. Hartmann, 2007: Testing the Fixed Anvil Temperature Hypothesis in a Cloud-Resolving Model. *J. Climate*, **20**, 2051–2057, https://doi.org/10.1175/JCLI4124.1.

Li, C., and A. Ingersoll, 2015: Moist convection in hydrogen atmospheres and the frequency of Saturn's giant storms. *Nature Geosci.*, **8**, 398–403, https://doi.org/10.1038/ngeo2405.

Li, Y., Y. Wang, and Z.-M. Tan, 2023: Is the outflow-layer inertial stability crucial to the energy cycle and development of tropical cyclones? *J. Atmos. Sci.*, https://doi.org/10.1175/JAS-D-22-0186.1.

Madhusudhan, N., M. C. Nixon, L. Welbanks, A. A. A. Piette, and R. A. Booth, 2020: The Interior and Atmosphere of the Habitable-zone Exoplanet K2-18b. *The Astrophysical Journal Letters*, **891**, L7, https://doi.org/10.3847/2041-8213/ab7229.

Mahrt, L. T., and J. Sun, 1995: The subgrid velocity scale in the bulk aerodynamic relationship for spatially averaged scalar fluxes. *Mon. Wea. Rev.*, **123**, 3032–3041, https://doi.org/10.1175/1520-0493(1995)123⟨3032:TSVSIT⟩2.0.CO;2.

Mansell, E., and C. L. Ziegler, 2010: Aerosol Effects on Simulated Storm Electrification and Precipitation in a Two-Moment Bulk Microphysics Model. *J. Atmos. Sci.*, **70**, 2032–2050, https://doi.org/10.1175/JAS-D-12-0264.1.

Mansell, E., C. L. Ziegler, and E. C. Bruning, 2010: Simulated Electrification of a Small Thunderstorm with Two-Moment Bulk Microphysics. *J. Atmos. Sci.*, **67**, 171–194, https://doi.org/10.1175/2009JAS2965.1.

Marquet, P., 2011: Definition of a moist entropy potential temperature: application to FIRE-I data flights. *Quart. J. Roy. Meteor. Soc.*, **137**, 768–791, https://doi.org/10.1002/qj.787.

Marquet, P., 2017: A third-law isentropic analysis of a simulated hurricane. *J. Atmos. Sci.*, **74**, 3451–3471, https://doi.org/10.1175/JAS-D-17-0126.1.

McColl, K. A., and L. I. Tang, 2024: An Analytic Theory of Near-Surface Relative Humidity over Land. *J. Climate*, **37**, 1213–1230, https://doi.org/10.1175/JCLI-D-23-0342.1.

McKinney, M. M., and J. Mitchell, 2024: Seasons, Shorelines, and Their Effects on the Tropical Circulation and Hydrological Cycle. *J. Atmos. Sci.*, **81**, 1475–1494, https://doi.org/10.1175/JAS-D-23-0076.1.

McKinney, M. M., J. Mitchell, and S. I. Thomson, 2022: Effects of Varying Land Coverage, Rotation Period, and Water Vapor on Equatorial Climates that Bridge the Gap between Earth-like and Titan-like. *J. Atmos. Sci.*, **79**, 2813–2830, https://doi.org/10.1175/JAS-D-21-0295.1.

Mikal-Evans, T., N. Madhusudhan, J. Dittmann, M. N. Günther, L. Welbanks, V. V. Eylen, I. J. M. C. T. Daylan, and L. Kreidberg, 2023: Hubble Space Telescope Transmission Spectroscopy for the Temperate Sub-Neptune TOI-270 d: A Possible Hydrogen-rich Atmosphere Containing Water Vapor. *The Astronomical Journal*, **165**, 84, https://doi.org/10.3847/1538-3881/aca90b.

Mitchell, J., 2008: The drying of Titan's dunes: Titan's methane hydrology and its impact on atmospheric circulation. *J. Geophys. Res.*, **113**, E08 015, https://doi.org/10.1029/2007JE003017.

Mitchell, J., and J. M. Lora, 2016: The Climate of Titan. *Annual Review of Earth and Planetary Sciences*, **44**, 353–380, https://doi.org/10.1146/annurev-earth-060115-012428.

Mitchell, J., R. Pierrehumbert, D. Frierson, and R. Caballero, 2006: The dynamics behind Titan's methane clouds. *Proc. Natl. Acad. Sci. (USA)*, **103**, 18 421–18 426, https://doi.org/10.1073/pnas.0605074103.

Mitchell, J., R. Pierrehumbert, D. Frierson, and R. Caballero, 2009: The impact of methan thermodynamics on seasonal convection and circulation in a model Titan atmosphere. *Icarus*, **203**, 250–264, https://doi.org/10.1016/j.icarus.2009.03.043.

Morrison, H., J. A. Curry, and V. I. Khvorostyanov, 2005: A New Double-Moment Microphysics Parameterization for Application in Cloud and Climate Models. Part I: Description. *J. Atmos. Sci.*, **62**, 1665–1677, https://doi.org/10.1175/JAS3446.1.

Morrison, H., G. Thompson, and V. Tatarskii, 2009: Impact of Cloud Microphysics on the Development of Trailing Stratiform Precipitation in a Simulated Squall Line: Comparison of One- and Two-Moment Schemes. *Mon. Wea. Rev.*, **137**, 991–1007, https://doi.org/10.1175/2008MWR2556.1.

Mrowiec, A. A., S. T. Garner, and O. M. Pauluis, 2011: Axisymmetric Hurricane in a Dry Atmosphere: Theoretical Framework and Numerical Experiments. *J. Atmos. Sci.*, **68**, 1607–1619, https://doi.org/10.1175/2011JAS3639.1.

Mrowiec, A. A., O. M. Pauluis, A. M. Frindlind, and A. S. Ackerman, 2015: Properties of a Mesoscale Convective System in the Context of an Isentropic Analysis. *J. Atmos. Sci.*, **72**, 1945–1962, https://doi.org/10.1175/JAS-D-14-0139.1.

Mrowiec, A. A., O. M. Pauluis, and F. Zhang, 2016: Isentropic Analysis of a Simulated Hurricane. *J. Atmos. Sci.*, **73**, 1857–1870, https://doi.org/10.1175/JAS-D-15-0063.1.

Muller, C. J., and I. M. Held, 2012: Detailed Investigation of the Self-Aggregation of Convection in Cloud-Resolving Simulations. *J. Atmos. Sci.*, **69**, 2551–2565, https://doi.org/10.1175/JAS-D-11-0257.1.

Muller, C. J., and D. M. Romps, 2018: Acceleration of tropical cyclogenesis by self-aggregation feedbacks. *Proc. Natl. Acad. Sci. (USA)*, **115**, 2930–2935, https://doi.org/10.1073/pnas.1719967115.

Nakanishi, M., and H. Niino, 2006: An Improved Mellor–Yamada Level-3 Model: Its Numerical Stability and Application to a Regional Prediction of Advection Fog. *Boundary-Layer Meteorol.*, **119**, 397–407, https://doi.org/10.1007/s10546-005-9030-8.

Nakanishi, M., and H. Niino, 2009: Development of an Improved Turbulence Closure Model for the Atmospheric Boundary Layer. *J. Meteor. Soc. Japan*, **87**, 895–912, https://doi.org/10.2151/jmsj.87.895.

Olson, J. B., J. S. Kenyon, W. M. Angevine, J. M. . Brown, M. Pagowski, and K. Sušelj, 2019: A Description of the MYNN-EDMF Scheme and the Coupling to Other Components in WRF–ARW. *NOAA Technical Memorandum OAR GSD*, **61**, 37, https://doi.org/10.25923/n9wm-be49.

O'Neill, M., and D. R. Chavas, 2020: Inertial Waves in Axisymmetric Tropical Cyclones. *J. Atmos. Sci.*, **77**, 2501–2517, https://doi.org/10.1175/JAS-D-19-0330.1.

Pauluis, O., and I. M. Held, 2002a: Entropy Budget of an Atmosphere in Radiative–Convective Equilibrium. Part I: Maximum Work and Frictional Dissipation. *J. Atmos. Sci.*, **59**, 125–139, https://doi.org/10.1175/1520-0469(2002)059⟨0125:EBOAAI⟩2.0.CO;2.

Pauluis, O., and I. M. Held, 2002b: Entropy Budget of an Atmosphere in Radiative–Convective Equilibrium. Part II: Latent Heat Transport and Moist Processes. *J. Atmos. Sci.*, **59**, 140–149, https://doi.org/10.1175/1520-0469(2002)059⟨0140:EBOAAI⟩2.0.CO;2.

Pauluis, O. M., 2000: Entropy budget of an atmosphere in radiative–convective equilibrium. Ph.D. thesis, Princeton University.

Pauluis, O. M., 2011: Water Vapor and Mechanical Work: A Comparison of Carnot and Steam Cycles. *J. Atmos. Sci.*, **68**, 91–102, https://doi.org/10.1175/2010JAS3530.1.

Pauluis, O. M., 2016: The Mean Air Flow as Lagrangian Dynamics Approximation and Its Application to Moist Convection. *J. Atmos. Sci.*, **73**, 4407–4425, https://doi.org/10.1175/JAS-D-15-0284.1.

Pauluis, O. M., and A. A. Mrowiec, 2013: Isentropic Analysis of Convective Motions. *J. Atmos. Sci.*, **70**, 3673–3688, https://doi.org/10.1175/JAS-D-12-0205.1.

Pauluis, O. M., and F. Zhang, 2017: Reconstruction of Thermodynamic Cycles in a High-Resolution Simulation of a Hurricane. *J. Atmos. Sci.*, **74**, 3367–3381, https://doi.org/10.1175/JAS-D-16-0353.1.

Piaulet, C., and Coauthors, 2023: Evidence for the volatile-rich composition of a 1.5-Earth-radius planet. *Nat. Astron.*, **7**, 206–222, https://doi.org/10.1038/s41550-022-01835-4.

Piaulet-Ghorayeb, C., and Coauthors, 2024: JWST/NIRISS Reveals the Water-rich "Steam World" Atmosphere of GJ 9827 d. *The Astrophysical Journal Letters*, **974**, L10, https://doi.org/10.3847/2041-8213/ad6f00.

Pierrehumbert, R. T., and F. Ding, 2016: Dynamics of atmospheres with a non-dilute condensible component. *Proc. Roy. Soc. A: Mathematical, Physical and Engineering Sciences*, **472**, 20160 107, https://doi.org/10.1098/rspa.2016.0107.

Régibeau-Rockett, L., 2025: Thermodynamic behavior of atmospheric heat engines in different environments. Ph.D. thesis, Stanford University.

Régibeau-Rockett, L., O. M. Pauluis, and M. E. O'Neill, 2024: Investigating the Relationship between Sea Surface Temperature and the Mechanical Efficiency of Tropical Cyclones. *J. Climate*, **37**, 439–456, https://doi.org/10.1175/JCLI-D-22-0877.1.

Rennó, N. O., and A. P. Ingersoll, 1996: Natural convection as a heat engine: A theory for CAPE. *J. Atmos. Sci.*, **53**, 572–585, https://doi.org/10.1175/1520-0469(1996)053⟨0572:NCAAHE⟩2.0.CO;2.

Rochetin, N., B. R. Lintner, K. L. Findell, A. H. Sobel, and P. Gentine, 2014: Radiative–Convective Equilibrium over a Land Surface. *J. Climate*, **27**, 8611–8629, https://doi.org/10.1175/JCLI-D-13-00654.1.

Roy, P.-A., and Coauthors, 2023: Water Absorption in the Transmission Spectrum of the Water World Candidate GJ 9827 d. *The Astrophysical Journal Letters*, **954**, L52, https://doi.org/10.3847/2041-8213/acebf0.

Seeley, J. T., N. Jeevanjee, and D. M. Romps, 2019: FAT or FiTT: Are anvil clouds or the tropopause temperature invariant? *Geophys. Res. Lett.*, **46**, 1842–1850, https://doi.org/10.1029/2018GL080096.

Seidel, D. J., Y. Zhang, A. Beljaars, J.-C. Golaz, A. R. Jacobson, and B. Medeiros, 2012: Climatology of the planetary boundary layer over the continental United States and Europe. *J. Geophys. Res.*, **117**, D17 106, https://doi.org/10.1029/2012JD018143.

Singh, M. S., and P. A. O'Gorman, 2015: Increases in moist-convective updraught velocities with warming in radiative-convective equilibrium. *Quart. J. Roy. Meteor. Soc.*, **141**, 2828–2838, https://doi.org/10.1002/qj.2567.

Singh, M. S., and P. A. O'Gorman, 2016: Scaling of the entropy budget with surface temperature in radiative-convective equilibrium. *Journal of Advances in Modeling Earth Systems*, **8**, 1132–1150, https://doi.org/10.1002/2016MS000673.

Singh, M. S., and M. E. O'Neill, 2022: The climate system and the second law of thermodynamics. *Rev. Mod. Phys.*, **94**, 015 001, https://doi.org/10.1103/RevModPhys.94.015001.

Skamarock, W. C., and Coauthors, 2008: A description of the advanced research WRF version 3. Tech. rep., National Center for Atmospheric Research, Boulder, Colorado, USA.

Southworth, J., L. Mancini, N. Madhusudhan, P. Mollière, S. Ciceri, and T. Henning, 2017: Detection of the Atmosphere of the 1.6 $M_{\oplus}$ Exoplanet GJ 1132 b. *The Astronomical Journal*, **153**, 191, https://doi.org/10.3847/1538-3881/aa6477.

Spaulding-Astudillo, F. E., and J. L. Mitchell, 2023: Effects of Varying Saturation Vapor Pressure on Climate, Clouds, and Convection. *J. Atmos. Sci.*, **80**, 1247–1266, https://doi.org/10.1175/JAS-D-22-0063.1.

Thompson, D. W. J., S. Bony, and Y. Li, 2017: Thermodynamic constraint on the depth of the global tropospheric circulation. *Proc. Natl. Acad. Sci. (USA)*, **114**, 8181–8186, https://doi.org/10.1073/pnas.1620493114.

Thompson, G., and T. Eidhammer, 2014: A Study of Aerosol Impacts on Clouds and Precipitation Development in a Large Winter Cyclone. *J. Atmos. Sci.*, **71**, 3636–3658, https://doi.org/10.1175/JAS-D-13-0305.1.

Thompson, G., P. R. Field, R. M. Rasmussen, and W. D. Hall, 2008: Explicit Forecasts of Winter Precipitation Using an Improved Bulk Microphysics Scheme. Part II: Implementation of a New Snow Parameterization. *Mon. Wea. Rev.*, **136**, 5095–5115, https://doi.org/10.1175/2008MWR2387.1.

Thuburn, J., and G. C. Craig, 2002: On the temperature structure of the tropical substratosphere. *J. Geophys. Res.*, **107**, https://doi.org/10.1029/2001JD000448.

Tobin, I., S. Bony, and R. Roca, 2012: Observational Evidence for Relationships between the Degree of Aggregation of Deep Convection, Water Vapor, Surface Fluxes, and Radiation. *J. Climate*, **25**, 6885–6904, https://doi.org/10.1175/JCLI-D-11-00258.1.

Tompkins, A. M., and A. G. Semie, 2017: Organization of tropical convection in low vertical wind shears: Role of updraft entrainment. *J. Adv. Model. Earth Syst.*, **9**, 1046–1068, https://doi.org/10.1002/2016MS000802.

Tsiaras, A., I. P. Waldmann, G. Tinetti, J. Tennyson, and S. N. Yurchenko, 2019: Water vapour in the atmosphere of the habitable-zone eight-Earth-mass planet K2-18 b. *Nat. Astron.*, **3**, 1086–1091, https://doi.org/10.1038/s41550-019-0878-9.

Urata, R. A., and O. B. Toon, 2013: Simulations of the martian hydrologic cycle with a general circulation model: Implications for the ancient martian climate. *Icarus*, **226**, 229–250, https://doi.org/10.1016/j.icarus.2013.05.014.

van der Drift, R. T., and P. A. O'Gorman, 2025: Dependence of Convective Precipitation Extremes on Near-Surface Relative Humidity. *J. Climate*, **38**, 6207–6225, https://doi.org/10.1175/JCLI-D-24-0738.1.

von Engeln, A., and J. Teixeira, 2013: A Planetary Boundary Layer Height Climatology Derived from ECMWF Reanalysis Data. *J. Climate*, **26**, 6575–6590, https://doi.org/10.1175/JCLI-D-12-00385.1.

Wang, D., and Y. Lin, 2020: Size and Structure of Dry and Moist Reversible Tropical Cyclones. *J. Atmos. Sci.*, **77**, 2091–2114, https://doi.org/10.1175/JAS-D-19-0229.1.

Wang, D., and Y. Lin, 2021: Potential Role of Irreversible Moist Processes in Modulating Tropical Cyclone Surface Wind Structure. *J. Atmos. Sci.*, **78**, 709–725, https://doi.org/10.1175/JAS-D-20-0192.1.

Wilhelmson, R. B., and C.-S. Chen, 1982: A Simulation of the Development of Successive Cells Along a Cold Outflow Boundary. *J. Atmos. Sci.*, **39**, 1466–1483, https://doi.org/10.1175/1520-0469(1982)039⟨1466:ASOTDO⟩2.0.CO;2.

Wing, A. A., and T. W. Cronin, 2016: Self-aggregation of convection in long channel geometry. *Quart. J. Roy. Meteor. Soc,*, **142**, 1–15, https://doi.org/10.1002/qj.2628.

WMO, 1957: Meteorology-A three-dimensional science: Second session of the commission for aerology. *WMO Bull.*, **4**, 134–138.

Wordsworth, R., F. Forget, E. Millour, J. W. Head, J.-B. Madeleine, and B. Charnay, 2013: Global modelling of the early martian climate under a denser CO2 atmosphere: Water cycle and ice evolution. *Icarus*, **222**, 1–19, https://doi.org/10.1016/j.icarus.2012.09.036.

Xian, T., and C. R. Homeyer, 2019: Global tropopause altitudes in radiosondes and reanalyses. *Atmos. Chem. Phys.*, **19**, 5661–5678, https://doi.org/10.5194/acp-19-5661-2019.

Xu, K., T. Wong, B. A. Wielicki, L. Parker, and Z. A. Eitzen, 2005: Statistical Analyses of Satellite Cloud Object Data from CERES. Part I: Methodology and Preliminary Results of the 1998 El Niño/2000 La Niña. *J. Climate*, **18**, 2497–2514, https://doi.org/10.1175/JCLI3418.1.

Zelinka, M. D., and D. L. Hartmann, 2010: Why is longwave cloud feedback positive? *J. Geophys. Res.*, **115**, D16 117, https://doi.org/10.1029/2010JD013817.

Zhang, Y., K. Sun, Z. Gao, Z. Pan, M. A. Shook, and D. Li, 2020: Diurnal climatology of planetary boundary layer height over the contiguous United States derived from AMDAR and reanalysis data. *J. Geophys. Res. Atmos.*, **125**, e2020JD032 803, https://doi.org/10.1029/2020JD032803.

Ziegler, C. L., 1985: Retrieval of Thermal and Microphysical Variables in Observed Convective Storms. Part 1: Model Development and Preliminary Testing. *J. Atmos. Sci.*, **42**, 1487–1509, https://doi.org/10.1175/1520-0469(1985)042⟨1487:ROTAMV⟩2.0.CO;2.

Zsom, A., L. Kaltenegger, and C. Goldblatt, 2012: A 1d microphysical cloud model for Earth, and Earth-like exoplanets: Liquid water and water ice clouds in the convective troposphere. *Icarus*, **221**, 603–616, https://doi.org/10.1016/j.icarus.2012.08.028.